

An Arbitrary High Order Discontinuous Galerkin Method for Elastic Waves on Unstructured Meshes I: The Two-Dimensional Isotropic Case

Martin Käser¹, Michael Dumbser¹

¹ *Department of Civil and Environmental Engineering, University of Trento, Trento, Italy*

Accepted 1999 November 11. Received 1999 October 6; in original form 1999 August 3

SUMMARY

We present a new numerical approach to solve the elastic wave equation in heterogeneous media with arbitrary high order accuracy in space and time on unstructured triangular meshes. We combine a Discontinuous Galerkin Method with the ideas of the ADER time integration approach using arbitrary high order derivatives. In contrast to classical finite element methods we allow for discontinuities of the piecewise polynomial approximation of the solution at element interfaces. This way, we can use the well-established theory of fluxes across element interfaces based on the solution of Riemann problems as developed in the finite volume framework. In particular, we replace time derivatives in the Taylor expansion of the time integration procedure by space derivatives to obtain a numerical scheme of the same high order in time and space automatically. The method is specially suited for linear hyperbolic systems such as the heterogeneous elastic wave equations and allows an efficient implementation. The convergence analysis demonstrates that very high accuracy is retained even on strongly irregular meshes and by increasing the order of the ADER-Discontinuous Galerkin schemes computational time and storage space can be reduced drastically. Applications of the proposed method to a problem of strong material heterogeneities and to the problem of global seismic wave propagation finally confirm its robustness and high flexibility.

Key words: elastic waves, discontinuous Galerkin method, arbitrary high order, unstructured mesh

1 INTRODUCTION

The accurate simulation of elastic wave propagation in heterogeneous media with complicated geometry is still a challenging task. Unstructured meshes that can be adapted to difficult geometrical models often lead to less accurate numerical schemes. However, as the waveforms contain important information about the interior structure of a material, it is necessary to develop numerical methods that are capable of computing accurate solutions, e.g. seismograms of high frequencies, even on such strongly irregular meshes that may arise when complex geometries have to be meshed. Furthermore highly accurate numerical schemes serve to eliminate as far as possible the errors introduced purely by the numerical approximation of the underlying physical model such that the misfit of simulated and measured data should only become due to errors in the mathematical description of the physical problem or due to incorrect initialization of the physical parameters of the investigated model and not due to insufficient accuracy of the numerical method that is used.

In the past two decades a variety of different numerical schemes has been developed in order to solve the elastic wave equations. Finite difference (FD) schemes for the simulation of SH and P-SV waves on regular, staggered grids were introduced by Virieux (1984; 1986). Later these schemes were extended to higher orders (Levander 1988), three dimensions (Moczo *et al.* 2002; Mora 1989) and anisotropic material (Igel, Mora & Riollot 1995; Tessmer 1995). FD like methods on unstructured meshes were developed in (Käser & Igel 2001a; Käser & Igel 2001b)

Alternatively pseudospectral (PS) methods (Fornberg 1996) have been developed by Carcione (1994) and applied in (Igel 1999; Tessmer & Kosloff 1994), where the space dependent variables are expanded in a set of orthogonal basis functions which are known exactly at discrete locations and which also allow the accurate computation of derivatives. Furthermore, no grid-staggering is needed, which provides advantages when modeling anisotropic material. However, quite regular meshes have to be used and due to the global character of the derivative operators parallelisation is cumbersome.

Recently the spectral element method (SEM), originally introduced by Patera (1984) in the field of computational fluid mechanics, gained increasing popularity in numerical seismology. SEM for elastic wave propagation has been applied in two and three space dimensions (Komatitsch & Vilotte 1998; Priolo, Carcione & Seriani 1994; Seriani 1998) and demonstrated advantages in particular for the problem of global wave propagation (Komatitsch & Tromp 1999; Komatitsch & Tromp 2002). The fundamental idea is to combine the advantages of a spectral method with those of a finite element (FE) method.

However, it is worth mentioning that all the above mentioned schemes usually use rather low order schemes for the time integration, e.g. second order Newmark-type schemes (Hughes 1987) or at most fourth order Runge-Kutta schemes (Igel 1999). Furthermore, we note that for wave propagation problems time accuracy is crucial, in particular when waves are propagating over many wavelengths, as shown in (Dumbser, Schwartzkopff & Munz).

Therefore, in this paper we present a new Discontinuous Galerkin (DG) finite element scheme for two space dimensions that uses the Arbitrary high order DERivatives (ADER) approach in order to solve the elastic wave equations with very high accuracy in both space *and* time. The proposed numerical method relies on the combination of the Discontinuous Galerkin finite element method and the ADER approach, originally developed by Toro *et al.* (2001) and Titarev & Toro (2002) and in (Schwartzkopff, Munz & Toro 2002; Schwartzkopff, Dumbser & Munz 2004) in the finite volume (FV) framework. The DG schemes belong to a quite recent class of numerical methods first used by Reed and Hill (1973) to solve linear neutron transport equations. As usual in the FE framework, the unknown solution is approximated inside each element by a polynomial, whose coefficients - the degrees of freedom - are advanced in time. In contrast to classical continuous FE, within the DG framework the solution can be *discontinuous* across the element interfaces, which allows to incorporate the well-established ideas of numerical flux functions from the finite volume framework. We especially point out that allowing jumps in the numerical solution may be very useful to capture large jumps in the material properties as will be shown in the first example of section 6. In the last decade mainly Cockburn and Shu (1989a; 1989b; 1990; 1991; 1998) put the DG scheme into a clear framework together with TVD-Runge-Kutta time integration methods.

Here, we present a theoretically arbitrary high order DG scheme in combination with the ADER approach in order to reach space and time accuracy of the same order. Furthermore, the method is formulated as a one step scheme, i.e. we do not need to compute and store intermediate stages as e.g. for Runge-Kutta methods to update the solution to the successive time level. The ADER-DG method proposed in this paper can handle unstructured triangular meshes and therefore is extremely flexible as far as computational domains with complicated geometrical structure are concerned. ADER-DG schemes were first developed for linear hyperbolic systems with constant coefficients or for linear systems with variable coefficients in conservative form (Dumbser 2003; Dumbser & Munz).

In this paper we consider the extension to non-conservative systems with variable coefficients such as the heterogeneous elastic wave equation. Furthermore, we point out that preliminary results of an extension of the method to three space dimensions as well as a parallel implementation of the ADER-DG scheme have already been achieved. However, the details of this will be subject to a further publication.

The paper is structured as follows. In Section 2 we introduce the system of the elastic wave equations in the non-conservative velocity-stress formulation. The proposed DG scheme is presented in Section 3 together with the ADER approach and an efficient formulation of the required Cauchy-Kovalewski procedure. In Section 4 we address boundary conditions for open and free-surface boundaries. After investigating numerically the convergence of the ADER-DG scheme in Section 5 on regular and very irregular triangular meshes, we show two applications of the new scheme in Section 6. One considers a test case for strong heterogeneities in elastic materials as suggested by LeVeque (2002), the other solves for the problem of global two-dimensional wave propagation using the radially symmetric Preliminary Reference Earth Model (PREM) of Dziewonski & Anderson (1981).

2 ELASTIC WAVE EQUATIONS

The propagation of waves in an elastic medium is based on the theory of linear elasticity (Aki & Richards 2002; Bedford & Drumheller 1994). Combining the definition of strain caused by deformations (Hooke's law) and the equations of the dynamic relationship between acceleration and stress, the elastic wave equations can be derived as shown in (LeVeque 2002). Considering the two-dimensional elastic wave equation for an isotropic medium in velocity-stress formulation leads to a linear hyperbolic system of the form

$$\begin{aligned}
 \frac{\partial}{\partial t} \sigma_{xx} - (\lambda + 2\mu) \frac{\partial}{\partial x} v - \lambda \frac{\partial}{\partial y} w &= 0, \\
 \frac{\partial}{\partial t} \sigma_{yy} - \lambda \frac{\partial}{\partial x} v - (\lambda + 2\mu) \frac{\partial}{\partial y} w &= 0, \\
 \frac{\partial}{\partial t} \sigma_{xy} - \mu \left(\frac{\partial}{\partial x} w + \frac{\partial}{\partial y} v \right) &= 0, \\
 \rho \frac{\partial}{\partial t} v - \frac{\partial}{\partial x} \sigma_{xx} - \frac{\partial}{\partial y} \sigma_{xy} &= 0, \\
 \rho \frac{\partial}{\partial t} w - \frac{\partial}{\partial x} \sigma_{xy} - \frac{\partial}{\partial y} \sigma_{yy} &= 0,
 \end{aligned} \tag{1}$$

where λ and μ are the *Lamé constants* and ρ is the mass density of the material. The normal stress components are given by σ_{xx} and σ_{yy} , and the shear stress is σ_{xy} . The components of the particle velocities in x - and y -direction are denoted by v and w , respectively. This system was already used in the seminal papers of Virieux (1984; 1986).

We remark that for notational simplicity, we skip the time and space dependencies of the variables. For the rest of this paper, the stresses and velocities are always assumed to be functions of time and space, i.e. $\sigma_{xx} = \sigma_{xx}(\vec{x}, t)$, $\sigma_{yy} = \sigma_{yy}(\vec{x}, t)$, $\sigma_{xy} = \sigma_{xy}(\vec{x}, t)$, $v = v(\vec{x}, t)$, $w = w(\vec{x}, t)$, with $t \in \mathbb{R}$ and $\vec{x} = (x, y)^T \in \mathbb{R}^2$. The physical properties of the material are functions of space but are constant in time, i.e. $\lambda = \lambda(\vec{x})$, $\mu = \mu(\vec{x})$, and $\rho = \rho(\vec{x})$, in order to describe heterogeneous material.

For the investigation of the eigenstructure of the system (1), we use the more compact form

$$\frac{\partial u_p}{\partial t} + A_{pq} \frac{\partial u_q}{\partial x} + B_{pq} \frac{\partial u_q}{\partial y} = 0, \quad (2)$$

where u is the vector of the p unknown variables, i.e. $u = (\sigma_{xx}, \sigma_{yy}, \sigma_{xy}, v, w)^T$. Here, we use classical tensor notation which implies summation over each index appearing twice. The matrices $A_{pq} = A_{pq}(\vec{x})$ and $B_{pq} = B_{pq}(\vec{x})$ are the space dependent Jacobian matrices of size $p \times q$, with $p, q = 1, \dots, 5$, as given by

$$A_{pq} = \begin{pmatrix} 0 & 0 & 0 & -(\lambda + 2\mu) & 0 \\ 0 & 0 & 0 & -\lambda & 0 \\ 0 & 0 & 0 & 0 & -\mu \\ -\frac{1}{\rho} & 0 & 0 & 0 & 0 \\ 0 & 0 & -\frac{1}{\rho} & 0 & 0 \end{pmatrix}, \quad (3)$$

$$B_{pq} = \begin{pmatrix} 0 & 0 & 0 & 0 & -\lambda \\ 0 & 0 & 0 & 0 & -(\lambda + 2\mu) \\ 0 & 0 & 0 & -\mu & 0 \\ 0 & 0 & -\frac{1}{\rho} & 0 & 0 \\ 0 & -\frac{1}{\rho} & 0 & 0 & 0 \end{pmatrix}. \quad (4)$$

In the framework of unstructured triangular meshes, where cell edges in general are not aligned with the coordinate axis, the Jacobian matrix $(A_n)_{pq}$ in normal direction $\vec{n} = (n_x, n_y)^T$ to a cell interface is obtained by the linear combination of the Jacobian matrices in (3) and (4)

$$\begin{aligned} (A_n)_{pq} &= n_x A_{pq} + n_y B_{pq} \\ &= \begin{pmatrix} 0 & 0 & 0 & -n_x(\lambda + 2\mu) & -n_y \lambda \\ 0 & 0 & 0 & -n_x \lambda & -n_y(\lambda + 2\mu) \\ 0 & 0 & 0 & -n_y \mu & -n_x \mu \\ -\frac{n_x}{\rho} & 0 & -\frac{n_y}{\rho} & 0 & 0 \\ 0 & -\frac{n_y}{\rho} & -\frac{n_x}{\rho} & 0 & 0 \end{pmatrix}. \end{aligned} \quad (5)$$

The propagation velocity of the elastic waves are determined by the eigenvalues of the Jacobian matrices A_{pq} and B_{pq} and result in

$$s_1 = -c_p, \quad s_2 = -c_s, \quad s_3 = 0, \quad s_4 = c_s, \quad s_5 = c_p, \quad (6)$$

where

$$c_p = \sqrt{\frac{\lambda + 2\mu}{\rho}}, \quad \text{and} \quad c_s = \sqrt{\frac{\mu}{\rho}}. \quad (7)$$

We remark that for the isotropic case the wave speeds in (6) and (7) do not depend on the propagation direction. The two P-waves propagate with speeds s_1 and s_5 and the two S-waves propagate with speeds s_2 and s_4 in the negative and positive direction with respect to \vec{n} .

$R_{p1}^{A_n}, \dots, R_{p5}^{A_n}$ denote the right eigenvectors of the normal Jacobian matrix in (5) in direction \vec{n} and are given by the columns of the matrix of right eigenvectors

$$R_{pq}^{A_n} = \begin{pmatrix} \lambda + 2\mu n_x^2 & -2\mu n_x n_y & n_y^2 & -2\mu n_x n_y & \lambda + 2\mu n_x^2 \\ \lambda + 2\mu n_y^2 & 2\mu n_x n_y & n_x^2 & 2\mu n_x n_y & \lambda + 2\mu n_y^2 \\ 2\mu n_x n_y & \mu(n_x^2 - n_y^2) & -n_x n_y & \mu(n_x^2 - n_y^2) & 2\mu n_x n_y \\ n_x c_p & -n_y c_s & 0 & n_y c_s & -n_x c_p \\ n_y c_p & n_x c_s & 0 & -n_x c_s & -n_y c_p \end{pmatrix}. \quad (8)$$

The derived eigenstructure of the elastic wave equations provides the necessary information to construct the ADER-DG scheme as described in the following Section 3.

3 THE NUMERICAL SCHEME

For the construction of the numerical scheme, we consider the general linear hyperbolic system of equations with variable coefficients as given in (2). The computational domain $\Omega \in \mathbb{R}^2$ is divided in conforming triangular elements $\mathcal{T}^{(m)}$ being addressed by a unique index (m) . Furthermore, we suppose the matrices A_{pq} and B_{pq} to be piecewise constant inside an element $\mathcal{T}^{(m)}$.

3.1 Semi-Discrete Form of the Scheme

The numerical solution u_h of equation (2) is approximated inside each triangle $\mathcal{T}^{(m)}$ by a linear combination of time independent polynomial basis functions $\Phi_l(\xi, \eta)$ of degree N with support $\mathcal{T}^{(m)}$ and with time dependent degrees of freedom $\hat{u}_{pl}^{(m)}(t)$:

$$\left(u_h^{(m)}\right)_p(\xi, \eta, t) = \hat{u}_{pl}^{(m)}(t)\Phi_l(\xi, \eta). \quad (9)$$

ξ and η are the coordinates in a reference element \mathcal{T}_E and are defined in (17) and (18). The approximation space is denoted by V_h . We use orthogonal basis functions Φ_k that rely on the ideas originally developed by Dubiner (1991) and which are given e.g. in the book of Cockburn, Karniadakis & Shu (2000). Multiplying (2) by a test function $\Phi_k \in V_h$ and integrating over a triangle $\mathcal{T}^{(m)}$ gives

$$\int_{\mathcal{T}^{(m)}} \Phi_k \frac{\partial u_p}{\partial t} dV + \int_{\mathcal{T}^{(m)}} \Phi_k \left(A_{pq} \frac{\partial u_q}{\partial x} + B_{pq} \frac{\partial u_q}{\partial y} \right) dV = 0. \quad (10)$$

Integration of (10) by parts then yields

$$\int_{\mathcal{T}^{(m)}} \Phi_k \frac{\partial u_p}{\partial t} dV + \int_{\partial\mathcal{T}^{(m)}} \Phi_k F_p^h dS - \int_{\mathcal{T}^{(m)}} \left(\frac{\partial \Phi_k}{\partial x} A_{pq} u_q + \frac{\partial \Phi_k}{\partial y} B_{pq} u_q \right) dV = 0 \quad (11)$$

where a numerical flux F_p^h has been introduced in the surface integral since u_h may be discontinuous at an element boundary. As we suppose rotational invariance of the system in (2) for the isotropic case, the flux can be derived for a coordinate system, which is aligned with the outward pointing unit normal vector \vec{n} of an element boundary. The required transformation (rotation) of the unknowns in vector u_p from the global Cartesian system to the vector u_q^n in a local normal, i.e. *edge-aligned*, coordinate system is given by

$$u_p = T_{pq} u_q^n \quad (12)$$

For the two-dimensional elastic wave equations the transformation matrix T_{pq} in (12) reads as

$$T_{pq} = \begin{pmatrix} n_x^2 & n_y^2 & -2n_x n_y & 0 & 0 \\ n_y^2 & n_x^2 & 2n_x n_y & 0 & 0 \\ n_x n_y & -n_x n_y & n_x^2 - n_y^2 & 0 & 0 \\ 0 & 0 & 0 & n_x & -n_y \\ 0 & 0 & 0 & n_y & n_x \end{pmatrix}. \quad (13)$$

For the system in (2) we use the exact Riemann solver to compute the state at the cell interfaces by upwinding. The flux is then computed with the Jacobian matrix in 3, i.e. with the material properties given in the considered element. In the global Cartesian xy -system the numerical flux F_p^h in (11) for triangle $\mathcal{T}^{(m)}$ across the edge with one of the neighbour triangles $\mathcal{T}^{(m_j)}$, $j = 1, 2, 3$, is then given as

$$F_p^h = \frac{1}{2} T_{pq} \left(A_{qr}^{(m)} + \left| A_{qr}^{(m)} \right| \right) (T_{rs})^{-1} \hat{u}_{sl}^{(m)} \Phi_l^{(m)} + \frac{1}{2} T_{pq} \left(A_{qr}^{(m)} - \left| A_{qr}^{(m)} \right| \right) (T_{rs})^{-1} \hat{u}_{sl}^{(m_j)} \Phi_l^{(m_j)}, \quad (14)$$

where $\hat{u}_{sl}^{(m)} \Phi_l^{(m)}$ and $\hat{u}_{sl}^{(m_j)} \Phi_l^{(m_j)}$ are the boundary extrapolated values of the numerical solution from element $\mathcal{T}^{(m)}$ and the j -th side neighbour $\mathcal{T}^{(m_j)}$, respectively. The matrix $(T_{rs})^{-1}$ represents the back-transformation into the global xy -system. We point out that the boundary values of both elements adjacent to an interface contribute to the numerical flux. Furthermore, due to the rotation it is sufficient to evaluate the Jacobian matrix $A_{qr}^{(m)}$ in (3) in x -direction with the material properties given in triangle $\mathcal{T}^{(m)}$. This way, the numerical flux respects the non-conservative form of the governing equation in (2). The notation $\left| A_{qr}^{(m)} \right|$ of the absolute value of the Jacobian matrix has the meaning of applying the absolute value operator to the eigenvalues given in (6), i.e.

$$\left| A_{qr}^{(m)} \right| = R_{pr}^A |\Lambda_{rs}| \left(R_{sq}^A \right)^{-1}, \quad \text{with } |\Lambda_{rs}| = \text{diag}(|s_1|, |s_2|, \dots). \quad (15)$$

Now, inserting (9) and (14) into (11) and splitting the boundary integral into the contributions of each edge j of the triangle $\mathcal{T}^{(m)}$, we obtain

$$\begin{aligned} & \frac{\partial}{\partial t} \hat{u}_{pl}^{(m)} \int_{\mathcal{T}^{(m)}} \Phi_k \Phi_l dV + \\ & + \sum_{j=1}^3 T_{pq}^j \frac{1}{2} \left(A_{qr}^{(m)} + \left| A_{qr}^{(m)} \right| \right) (T_{rs}^j)^{-1} \hat{u}_{sl}^{(m)} \int_{(\partial\mathcal{T}^{(m)})_j} \Phi_k^{(m)} \Phi_l^{(m)} dS + \\ & + \sum_{j=1}^3 T_{pq}^j \frac{1}{2} \left(A_{qr}^{(m)} - \left| A_{qr}^{(m)} \right| \right) (T_{rs}^j)^{-1} \hat{u}_{sl}^{(m_j)} \int_{(\partial\mathcal{T}^{(m)})_j} \Phi_k^{(m)} \Phi_l^{(m_j)} dS - \\ & - A_{pq} \hat{u}_{ql}^{(m)} \int_{\mathcal{T}^{(m)}} \frac{\partial \Phi_k}{\partial x} \Phi_l dV - B_{pq} \hat{u}_{ql}^{(m)} \int_{\mathcal{T}^{(m)}} \frac{\partial \Phi_k}{\partial y} \Phi_l dV = 0. \end{aligned} \quad (16)$$

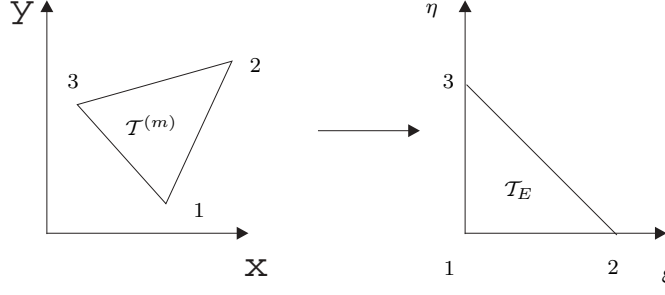


Figure 1. Transformation from the physical triangle $\mathcal{T}^{(m)}$ to the canonical reference triangle \mathcal{T}_E with nodes $(0, 0)$, $(1, 0)$ and $(0, 1)$.

Equation (16) is written in the global xy -system. If we transform each physical triangle $\mathcal{T}^{(m)}$ to a canonical reference triangle \mathcal{T}_E in a $\xi\eta$ -reference system as shown in Fig. 1, the method can be implemented much more efficiently since many integrals can be precomputed beforehand in this reference system. The coordinate transformation is defined by

$$\begin{aligned} x &= x_1 + (x_2 - x_1)\xi + (x_3 - x_1)\eta, \\ y &= y_1 + (y_2 - y_1)\xi + (y_3 - y_1)\eta, \end{aligned} \quad (17)$$

with the inverse transformation

$$\begin{aligned} \xi &= \frac{1}{|J|} \left((x_3 y_1 - x_1 y_3) + x(y_3 - y_1) + y(x_1 - x_3) \right), \\ \eta &= \frac{1}{|J|} \left((x_1 y_2 - x_2 y_1) + x(y_1 - y_2) + y(x_2 - x_1) \right), \end{aligned} \quad (18)$$

where $|J| = (x_2 - x_1)(y_3 - y_1) - (x_3 - x_1)(y_2 - y_1)$ is the determinant of the Jacobian matrix of the transformation being equal to the double of the triangle's surface.

With respect to the transformation, we have furthermore

$$dx dy = |J| d\xi d\eta, \quad (19)$$

and the transformed gradients

$$\begin{pmatrix} \frac{\partial}{\partial x} \\ \frac{\partial}{\partial y} \end{pmatrix} = \begin{pmatrix} \frac{\partial \xi}{\partial x} & \frac{\partial \eta}{\partial x} \\ \frac{\partial \xi}{\partial y} & \frac{\partial \eta}{\partial y} \end{pmatrix} \begin{pmatrix} \frac{\partial}{\partial \xi} \\ \frac{\partial}{\partial \eta} \end{pmatrix}. \quad (20)$$

Integrating in the reference system using (19) and (20), the semi-discrete DG formulation of (16) reads as

$$\begin{aligned} & \frac{\partial}{\partial t} \hat{u}_{pl}^{(m)} |J| \int_{\mathcal{T}_E} \Phi_k \Phi_l d\xi d\eta + \\ & + \sum_{j=1}^3 T_{pq}^j \frac{1}{2} \left(A_{qr}^{(m)} + |A_{qr}^{(m)}| \right) (T_{rs}^j)^{-1} \hat{u}_{sl}^{(m)} |S_j| \int_0^1 \Phi_k^{(m)}(\chi_j) \Phi_l^{(m)}(\chi_j) d\chi_j + \\ & + \sum_{j=1}^3 T_{pq}^j \frac{1}{2} \left(A_{qr}^{(m)} - |A_{qr}^{(m)}| \right) (T_{rs}^j)^{-1} \hat{u}_{sl}^{(m_j)} |S_j| \int_0^1 \Phi_k^{(m)}(\chi_j) \Phi_l^{(m_j)}(\chi_j) d\chi_j - \\ & - A_{pq}^* \hat{u}_{ql} |J| \int_{\mathcal{T}_E} \frac{\partial \Phi_k}{\partial \xi} \Phi_l d\xi d\eta - B_{pq}^* \hat{u}_{ql} |J| \int_{\mathcal{T}_E} \frac{\partial \Phi_k}{\partial \eta} \Phi_l d\xi d\eta = 0 \end{aligned} \quad (21)$$

with the special linear combination of the Jacobians

$$A_{pq}^* = A_{pq} \frac{\partial \xi}{\partial x} + B_{pq} \frac{\partial \xi}{\partial y}, \quad (22)$$

$$B_{pq}^* = A_{pq} \frac{\partial \eta}{\partial x} + B_{pq} \frac{\partial \eta}{\partial y}. \quad (23)$$

In (21) the variable $0 \leq \chi_j \leq 1$ is introduced to parameterize the j -th edge of the reference triangle and $|S_j|$ is the length of this edge in physical space. The following integrals

$$M_{kl} = \int_{\mathcal{T}_E} \Phi_k \Phi_l d\xi d\eta, \quad (24)$$

$$F_{kl}^{j,0} = \int_0^1 \Phi_k^{(m)}(\chi_j) \Phi_l^{(m)}(\chi_j) d\chi_j, \quad (25)$$

$$F_{kl}^{j,i} = \int_0^1 \Phi_k^{(m)}(\chi_j) \Phi_l^{(m_j)}(\chi_j) d\chi_j, \quad (26)$$

$$K_{kl}^\xi = \int_{\mathcal{T}_E} \frac{\partial \Phi_k}{\partial \xi} \Phi_l d\xi d\eta, \quad (27)$$

$$K_{kl}^\eta = \int_{\mathcal{T}_E} \frac{\partial \Phi_k}{\partial \eta} \Phi_l d\xi d\eta. \quad (28)$$

can all be calculated beforehand by a computer algebra system (e.g. Maple). On an unstructured mesh the flux matrices $F_{kl}^{j,0}$ account for the contribution of the element $\mathcal{T}^{(m)}$ itself to the fluxes over all three edges j and the flux matrices $F_{kl}^{j,i}$ account for the contribution of the elements' direct side neighbours $\mathcal{T}^{(m_j)}$ to the fluxes over the edges j . Index $1 \leq i \leq 3$ indicates the local number of the common edge in neighbour $\mathcal{T}^{(m_j)}$ and depends on the mesh generator. Matrices K_{kl}^ξ and K_{kl}^η are analogous to the stiffness matrices of classical continuous FE. We emphasize that for the DG method as given by (21) *no* assembly of global mass-, flux- and stiffness matrices is needed in contrast to continuous FE schemes. The method is completely local and therefore well suited for parallelization. Hence, there are no large global linear equation systems to solve and due to the choice of orthogonal basis functions the inversion of the diagonal DG mass matrix M_{kl} is trivial. Examples for matrices (24) to (28) can be found in (Dumbser & Munz). On a given mesh, where index i is known, only three of the nine possible matrices $F_{kl}^{j,i}$ are used per element.

If the semi-discrete equation (21) is integrated in time with a Runge-Kutta method, we obtain the quadrature-free Runge-Kutta Discontinuous Galerkin approach developed by Atkins & Shu (1998).

3.2 The ADER Time Discretization

Since the efficiency of Runge-Kutta (RK) time discretization schemes drastically decreases if the order of accuracy becomes greater than four, due to the so-called Butcher barriers (Butcher 1987) which cause the number of intermediate RK stages to become larger than the formal order of accuracy, we apply the ADER approach of Toro *et al.* (2001) to the semi-discrete form of the DG scheme (21) in order to achieve an arbitrarily accurate time discretization.

The main ingredients of the ADER approach (Toro & Titarev 2002) are a Taylor expansion in time, the solution of Derivative Riemann Problems (DRP) to approximate the space derivatives at the interface and the Cauchy-Kovalewski procedure for replacing the time derivatives in the Taylor series by space derivatives. In this section we show how the ADER approach can be used for high order time integration of the Discontinuous Galerkin method for linear hyperbolic systems and term the proposed scheme ADER-DG.

For the development of linear ADER-DG schemes, we first need a general formula for the Cauchy-Kovalewski procedure in order to replace the k -th time derivative by pure space derivatives. Since all our basis functions are given in the $\xi\eta$ -system, we need a Cauchy-Kovalewski procedure which makes use of the spatial derivatives with respect to ξ and η . Therefore, we rewrite our original PDE (2) with the use of (20) as

$$\frac{\partial u_p}{\partial t} + A_{pq} \left(\frac{\partial u_q}{\partial \xi} \frac{\partial \xi}{\partial x} + \frac{\partial u_q}{\partial \eta} \frac{\partial \eta}{\partial x} \right) + B_{pq} \left(\frac{\partial u_q}{\partial \xi} \frac{\partial \xi}{\partial y} + \frac{\partial u_q}{\partial \eta} \frac{\partial \eta}{\partial y} \right) = 0, \quad (29)$$

rearrange this equation to get

$$\frac{\partial u_p}{\partial t} + \left(A_{pq} \frac{\partial \xi}{\partial x} + B_{pq} \frac{\partial \xi}{\partial y} \right) \frac{\partial u_q}{\partial \xi} + \left(A_{pq} \frac{\partial \eta}{\partial x} + B_{pq} \frac{\partial \eta}{\partial y} \right) \frac{\partial u_q}{\partial \eta} = 0, \quad (30)$$

and finally, by using the definitions in (22) and (23), we obtain

$$\frac{\partial u_p}{\partial t} + A_{pq}^* \frac{\partial u_q}{\partial \xi} + B_{pq}^* \frac{\partial u_q}{\partial \eta} = 0. \quad (31)$$

The k -th time derivative as a function of pure space derivatives in the $\xi\eta$ -reference system is the result of the Cauchy-Kovalewski procedure applied to (31) and is given by

$$\frac{\partial^k u_p}{\partial t^k} = (-1)^k \left(A_{pq}^* \frac{\partial}{\partial \xi} + B_{pq}^* \frac{\partial}{\partial \eta} \right)^k u_q. \quad (32)$$

We point out that it is a key issue to use the Cauchy-Kovalewski procedure in the form (32) since it allows us to pre-calculate many matrices beforehand, as we will see in the following.

We develop the solution of (2) in a Taylor series in time up to order N ,

$$u_p(\xi, \eta, t) = \sum_{k=0}^N \frac{t^k}{k!} \frac{\partial^k}{\partial t^k} u_p(\xi, \eta, 0), \quad (33)$$

and replace time derivatives by space derivatives, using (32):

$$u_p(\xi, \eta, t) = \sum_{k=0}^N \frac{t^k}{k!} (-1)^k \left(A_{pq}^* \frac{\partial}{\partial \xi} + B_{pq}^* \frac{\partial}{\partial \eta} \right)^k u_q(\xi, \eta, 0). \quad (34)$$

We now introduce the Discontinuous Galerkin approximation (9) and obtain

$$u_p(\xi, \eta, t) = \sum_{k=0}^N \frac{t^k}{k!} (-1)^k \left(A_{pq}^* \frac{\partial}{\partial \xi} + B_{pq}^* \frac{\partial}{\partial \eta} \right)^k \Phi_l(\xi, \eta) \hat{u}_{ql}(0). \quad (35)$$

This approximation can now be projected onto each basis function in order to get an approximation of the evolution of the degrees of freedom during one time step from time level n to time level $n + 1$. We obtain

$$\hat{u}_{pl}(t) = \frac{\left\langle \Phi_n, \sum_{k=0}^N \frac{t^k}{k!} (-1)^k \left(A_{pq}^* \frac{\partial}{\partial \xi} + B_{pq}^* \frac{\partial}{\partial \eta} \right)^k \Phi_m(\xi) \right\rangle}{\langle \Phi_n, \Phi_l \rangle} \hat{u}_{qm}(0) \quad (36)$$

where $\langle \cdot, \cdot \rangle$ denotes the inner product over the reference triangle \mathcal{T}_E and the division by $\langle \Phi_n, \Phi_l \rangle$ denotes the multiplication with the inverse of the mass matrix. This reduces indeed to division by its diagonal entries since the mass matrix is diagonal due to the supposed orthogonality of the basis functions. Equation (36) can be integrated analytically in time and we obtain

$$\int_0^{\Delta t} \hat{u}_{pl}(t) dt = \frac{\left\langle \Phi_n, \sum_{k=0}^N \frac{\Delta t^{(k+1)}}{(k+1)!} (-1)^k \left(A_{pq}^* \frac{\partial}{\partial \xi} + B_{pq}^* \frac{\partial}{\partial \eta} \right)^k \Phi_m(\xi) \right\rangle}{\langle \Phi_n, \Phi_l \rangle} \hat{u}_{qm}(0). \quad (37)$$

With the definition

$$I_{plqm}(\Delta t) = \frac{\left\langle \Phi_n, \sum_{k=0}^N \frac{\Delta t^{(k+1)}}{(k+1)!} (-1)^k \left(A_{pq}^* \frac{\partial}{\partial \xi} + B_{pq}^* \frac{\partial}{\partial \eta} \right)^k \Phi_m(\xi) \right\rangle}{\langle \Phi_n, \Phi_l \rangle} \quad (38)$$

equation (37) becomes simply

$$\int_0^{\Delta t} \hat{u}_{pl}(t) dt = I_{plqm}(\Delta t) \hat{u}_{qm}(0) \quad (39)$$

and we finally obtain the fully discrete ADER-DG scheme by integration of (21) in time:

$$\begin{aligned} & \left[\left(\hat{u}_{pl}^{(m)} \right)^{n+1} - \left(\hat{u}_{pl}^{(m)} \right)^n \right] |J| M_{kl} + \\ & + \frac{1}{2} \sum_{j=1}^3 T_{pq}^j \left(A_{qr}^{(m)} + \left| A_{qr}^{(m)} \right| \right) (T_{rs}^j)^{-1} |S_j| F_{kl}^{j,0} \cdot I_{qlmn}(\Delta t) \left(\hat{u}_{mn}^{(m)} \right)^n + \\ & + \frac{1}{2} \sum_{j=1}^3 T_{pq}^j \left(A_{qr}^{(m)} + \left| A_{qr}^{(m)} \right| \right) (T_{rs}^j)^{-1} |S_j| F_{kl}^{j,i} \cdot I_{qlmn}(\Delta t) \left(\hat{u}_{mn}^{(m_j)} \right)^n - \\ & - A_{pq}^* |J| K_{kl}^\xi \cdot I_{qlmn}(\Delta t) \left(\hat{u}_{mn}^{(m)} \right)^n - B_{pq}^* |J| K_{kl}^\eta \cdot I_{qlmn}(\Delta t) \left(\hat{u}_{mn}^{(m)} \right)^n = 0. \end{aligned} \quad (40)$$

On rectangular elements, the scheme takes the same form except that one has to consider the contribution of four edges instead of three in the case of triangles. The equations (17) and (18) of the transformation remain unchanged, see (Schwarz 1988). The scheme is quadrature-free and performs high order time-integration from t^n to t^{n+1} in one single step. It thus needs the same memory as a first order explicit Euler time-stepping scheme. Note that for any DG scheme the initial condition at t^0 must be projected onto the degrees of freedom via L^2 projection.

3.3 An Efficient Algorithm for the Cauchy-Kovalewski Procedure of Linear Systems

On unstructured meshes, we must evaluate equation (38) in each triangle in each time step, if we do not want to store all the tensor coefficients $I_{plqm}(\Delta t)$ for each triangle. Therefore, in the following we show a very efficient algorithm for its evaluation on the reference cell. Equation (38) contains a binomial formula for matrices whose products unfortunately do not commute in the general case. If expanded explicitly, (38) becomes

$$I_{plqm}(\Delta t) = \langle \Phi_n, \Phi_l \rangle^{-1} \cdot \left\langle \Phi_n, \sum_{k=0}^N \frac{\Delta t^{(k+1)}}{(k+1)!} (-1)^k \times \sum_{n_B=0}^k S_{pq} \left(A_{pq}^*, B_{pq}^*, k - n_B, n_B \right) \frac{\partial^k}{\partial \xi^{(k-n_B)} \partial \eta^{n_B}} \Phi_m \right\rangle. \quad (41)$$

Hence, in the evaluation of (38) we have to compute the sums S_{pq} of all products of A_{pq}^* and B_{pq}^* in which matrix A_{pq}^* appears $n_A = k - n_B$ times and matrix B_{pq}^* appears n_B times, taking into account all possible matrix permutations. Without proof, we give a recursive algorithm defining the S_{pq} in step 1 of Algorithm 1. It recycles all previously computed data if implemented in an unrolled manner, storing intermediate results. In Algorithm 1, δ_{pq} denotes the usual Kronecker symbol.

Algorithm 1: (efficient Cauchy-Kovalewski procedure)

Step 1: Compute and store temporarily the sums of all matrix products of A_{pq}^* and B_{pq}^* with all possible permutations,

$$\begin{aligned} S_{pq}(A_{pq}^*, B_{pq}^*, n_A, n_B) &:= 0, & \text{if } n_A < 0 \vee n_B < 0, \\ S_{pq}(A_{pq}^*, B_{pq}^*, 0, 0) &:= \delta_{pq}, \\ S_{pq}(A_{pq}^*, B_{pq}^*, n_A, n_B) &= S_{pr}(A_{pr}^*, B_{pr}^*, n_A - 1, n_B) \cdot A_{rq}^* + \\ & \quad S_{pr}(A_{pr}^*, B_{pr}^*, n_A, n_B - 1) \cdot B_{rq}^*, \end{aligned}$$

$$\forall 0 \leq n_A + n_B \leq N.$$

Step 2: Exchange summation and integration in eqn. (41) and compute $I_{plqm}(\Delta t)$ as:

$$\begin{aligned} I_{plqm}(\Delta t) &= \sum_{k=0}^N \frac{\Delta t^{(k+1)}}{(k+1)!} (-1)^k \sum_{n_B=0}^k S_{pq}(A_{pq}^*, B_{pq}^*, k - n_B, n_B) \times \\ & \quad \langle \Phi_n, \Phi_l \rangle^{-1} \left\langle \Phi_n, \frac{\partial^k}{\partial \xi^{(k-n_B)} \partial \eta^{n_B}} \Phi_m \right\rangle. \end{aligned}$$

This algorithm is used in each triangle $\mathcal{T}^{(m)}$ in each time-step. However, all projections of the space derivatives of the basis functions onto all the test functions, as they appear in step 2 in Algorithm 1, can be precomputed once and then stored. They are defined on the canonical reference triangle and depend neither on the mesh nor on the time step.

4 BOUNDARY CONDITIONS

There is a variety of physically meaningful boundary conditions of an elastic medium. However, the two important types of boundaries are *open* and *free surface* boundaries.

4.1 Open Boundaries

At open boundaries, no waves are supposed to enter the computational domain and those waves that are travelling out should be able to pass the boundary without reflections. There is a whole scientific community dealing with non-reflective boundary conditions, however, in this section we present only a very simple approach that so far yielded satisfactory results, at least for our purposes. The numerical flux (14) is based on the solution of the Riemann-Problem given by the jump across the element interface. It is a strict upwind method, i.e. outgoing waves at an element interface are only influenced by the state in the element itself and not by the state in the neighbour. In contrast, the flux contribution of incoming waves is purely due to the state in the neighbour element. Thus, a very simple implementation of open boundary conditions is to use the following numerical flux in (40) at all those edges that coincide with an open boundary:

$$F_p^{\text{OpenBC}} = \frac{1}{2} T_{pq} \left(A_{qr}^{(m)} + \left| A_{qr}^{(m)} \right| \right) (T_{rs})^{-1} \hat{u}_{sl}^{(m)} \Phi_l^{(m)}. \quad (42)$$

The flux function (42) allows only for outgoing waves, which are merely defined by the state in the element due to upwinding. Since incoming waves are not allowed, the respective flux contribution must vanish.

4.2 Free Surface Boundaries

On the free surface of an elastic medium, the normal stress and the shear stresses with respect to the boundary are determined by physical constraints. At the outside of the elastic medium, there are no external forces that retract the particles into their original position. Therefore, the normal stress and the shear stress values at the free surface have to be zero. In contrast to classical continuous FE methods we have no direct control on the values at the boundaries within the Discontinuous Galerkin framework. However, the boundary values can be imposed via the numerical flux, as in the finite volume framework. Considering that the numerical flux is based on the solution of a Riemann-Problem at an element interface and given some boundary extrapolated values from inside the computational domain on a free surface, we must search corresponding virtual neighbour values *outside* the computational domain such that the solution of the Riemann-Problem yields exactly the free-surface boundary conditions *at* the domain boundary. However, the solution of this so-called inverse Riemann problem at a free surface boundary is quite simple and can be obtained via symmetry considerations. For those components of the state vector u_p , that we want to be zero at the domain boundary, we prescribe a virtual component outside the domain that has the same magnitude but opposite sign. For the other components we just copy the inside values to the virtual outside neighbour. For the free-surface boundary condition the resulting numerical flux function in (40) can then be formulated as follows,

$$\begin{aligned} F_p^{\text{FreeBC}} &= \frac{1}{2} T_{pq} \left(A_{qr}^{(m)} + \left| A_{qr}^{(m)} \right| \right) (T_{rs})^{-1} \hat{u}_{sl}^{(m)} \Phi_l^{(m)} + \\ & \quad + \frac{1}{2} T_{pq} \left(A_{qr}^{(m)} - \left| A_{qr}^{(m)} \right| \right) \Gamma_{rs} (T_{st})^{-1} \hat{u}_{tl}^{(m)} \Phi_l^{(m)}, \end{aligned} \quad (43)$$

where the matrix $\Gamma_{rs} = \text{diag}(-1, 1, -1, 1, 1)$ accounts for the mirroring of normal and shear stresses.

5 CONVERGENCE STUDY

In this section we numerically determine the convergence orders of the proposed ADER-DG schemes. As test case we solve the two-dimensional elastic wave equations in (1) on a square shaped domain $\Omega = [-50, 50] \times [-50, 50] \in \mathbb{R}^2$. We consider the initial condition

$$Q_p^0 = Q_p(\vec{x}, 0) = R_{p2}^{A_n} \sin(\vec{k} \cdot \vec{x}) + R_{p5}^{A_n} \sin(\vec{k} \cdot \vec{x}), \quad (44)$$

with the wave number

$$\vec{k} = (k_x, k_y)^T = \frac{2\pi}{25}(1, 1)^T. \quad (45)$$

The vectors $R_{p2}^{A_n}$ and $R_{p5}^{A_n}$ are two of the eigenvectors in (8). Therefore, the initial condition in (44) creates a plane sinusoidal P-wave traveling along the diagonal direction $\vec{n} = (1, 1)^T$, as well as a plane sinusoidal S-wave traveling into the opposite direction.

The homogeneous material parameters are set to

$$\lambda = 2, \quad \mu = 1, \quad \rho = 1, \quad (46)$$

throughout the computational domain Ω leading to the constant wave propagation velocities

$$c_p = 2, \quad c_s = 1, \quad (47)$$

for the P- and S-wave, respectively. The total simulation time T is set to $T = 100\sqrt{2}$, such that the P- and S-waves at simulation time $t = T$ coincide with the initial condition at time $t = 0$. Therefore, the exact reference solution is given by the initial condition in (44), i.e.

$$Q_p(\vec{x}, T) = Q_p(\vec{x}, 0). \quad (48)$$

The CFL number is set in all computations to 50% of the stability limit $\frac{1}{2N+1}$ of Runge-Kutta DG schemes. For a thorough investigation of the linear stability properties of the ADER-DG schemes via a von Neumann analysis see (Dumbser 2005).

The numerical experiments to determine the convergence orders are performed on two sequences of regular and irregular triangular meshes. Each sequence consists of four meshes with decreasing mesh width. The first two meshes of each sequence are shown in Fig. 2.

For the regular mesh the refinement is simply controlled by changing the number of grid cells in each dimension. For the irregular meshes we use the so-called *red-refinement* as described in detail in (Hempel 1995; Meister & Struckmeier 2002). As shown in Fig. 2 c) and d) each triangle is refined subsequently by dividing it into four similar sub triangles. We characterize the refinement state of a mesh by the maximum diameter h of the circumscribed circles of all triangular cells.

In Tables 1 and 2 the errors in L^∞ and L^2 norm are given in relation to h for the regular and irregular meshes. The corresponding numerical convergence orders \mathcal{O}_{L^∞} and \mathcal{O}_{L^2} are determined by two successively refined meshes. Furthermore, we present the total number N_d of degrees of freedom, which is a measure of required storage space during runtime. The computations were carried out on a Pentium Xeon 3.6 GHz processor with 4GB of RAM and the obtained CPU-times in seconds are also listed in Tables 1 and 2.

Based on these convergence results, we state that the proposed ADER-DG schemes achieve the expected convergence orders on both regular and irregular meshes. We note that the ADER-DG $\mathcal{O}10$ schemes for the finest meshes in both cases, regular and irregular, seem to reach machine precision. Therefore, the convergence orders slightly drop below the expected values. Also we mention that the CPU-time to reach the final simulation time $t = T$ is much larger for the irregular meshes. This is due to the small time steps caused by the CFL condition of the smallest diameter of the inscribed circle of all triangles (see Fig. 2 c) and d).

A visual comparison of the obtained results is given in Fig. 3 and 4. We plot the errors in L^∞ norm against mesh spacing h , total number of degrees of freedom N_d , and CPU-time. The slopes of the top plots in Fig. 3 and 4 give the convergence orders and show that with mesh refinement the errors decrease much faster if the order of the scheme is increased.

Similarly, for a desired maximum error the total number of degrees of freedom, which is directly proportional to the required storage space, decreases for higher order schemes. Or, in other words, for a given storage space higher accuracy can be reached with higher order schemes. In the last plot, we demonstrate that the CPU-time needed to reach a desired accuracy also decreases when using higher order schemes, in particular on the regular meshes. For the irregular meshes, the results are less clear for rather low accuracy requirements, e.g. $L^\infty > 10^{-3}$. However, if higher accuracy, e.g. $L^\infty < 10^{-3}$, is desired, the higher order schemes require significantly less CPU-time. Therefore, the results of the convergence analysis clearly demonstrate the advantages of high order ADER-DG schemes, when applied to the elastic wave equations. We also note that these results extend to other linear hyperbolic systems, such as the linearized Euler equations, as shown in (Dumbser 2005).

6 NUMERICAL EXAMPLES

Here we present two numerical examples in order to demonstrate the performance and flexibility of the proposed ADER-DG scheme.

In the first example we reproduce the results published in the book of LeVeque (2002) in order to show how large contrasts in material parameters of a heterogeneous medium can be easily handled. Furthermore, we clearly demonstrate that higher order schemes pay off, when high resolution results are required.

In the second example we apply our scheme to the case of global seismic wave propagation, where the advantages of flexible, triangular meshes are presented. Using an unstructured mesh we can easily overcome the problem of decreasing cell spacing towards the earth's center

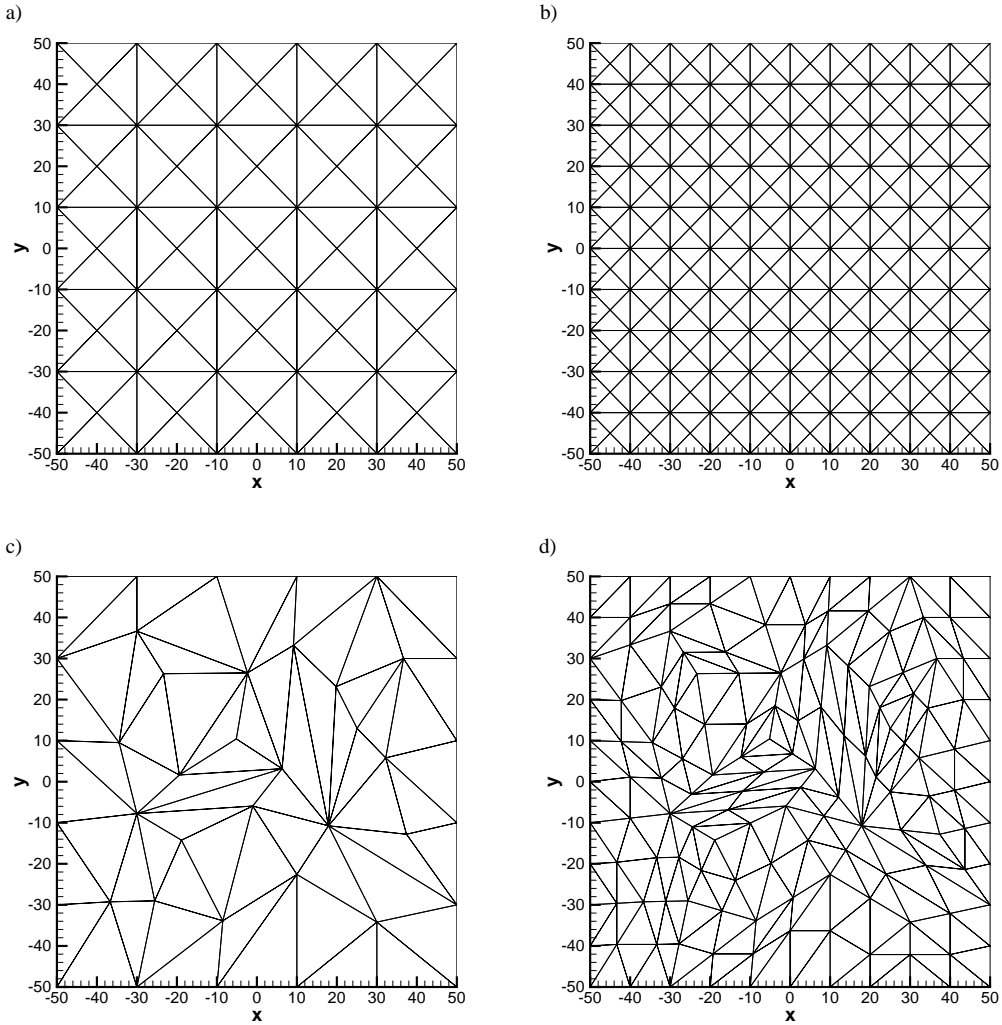


Figure 2. Meshes for the analysis of the numerical convergence orders: a) regular mesh, b) refined regular mesh c) irregular mesh, d) refined irregular mesh.

that usually arises when working with regular, structured grids e.g. for FD methods. In addition, we adjust the mesh spacing in a way to optimally make use of the CFL criterion, i.e. larger cells are used in zones of higher velocity, where the expected wavelengths are larger and thus cell sizes can be increased.

6.1 Example 1

The following numerical example is based on a test case given by LeVeque (2002) in Chapter 22.7. An initially plane P-wave travels through a heterogeneous elastic medium. The medium consists of two different materials where in an outer solid material of extent $\Omega_o = [-1, 1] \times [-0.5, 0.5]$ is embedded another, stiffer, elastic material of size $\Omega_i = [-0.5, 0.5] \times [-0.1, 0.1]$. The elastic properties of the outer material are $\rho_o = 1$, $\lambda_o = 2$, and $\mu_o = 1$, whereas the inner material has the properties $\rho_i = 1$, $\lambda_i = 200$, and $\mu_i = 100$. Therefore, we have to deal with a large jump of the physical parameters at the interface between the two materials. The wave speeds of both P- and S-waves inside the stiffer material are ten times larger than in the outer medium.

At the left and right boundaries ($x = \pm 1$) of Ω_o we implemented open boundaries, whereas at the top and bottom boundaries ($y = \pm 0.5$) we use a free surface boundary condition, where the normal stress σ_{yy} and the shear stress σ_{xy} must vanish.

The initial condition is given by

$$Q_p^0 = Q_p(\vec{x}, 0) = R_{p5}^{A_n} \exp\left(-\frac{1}{2} \frac{(x - x_0)^2}{\sigma^2}\right), \quad (49)$$

with $\vec{n} = (1, 0)^T$, $x_0 = -0.8$ and standard deviation $\sigma = 0.01$, which represents a plane P-wave of Gaussian shape travelling in x -direction. Initially, the center of the plane wave is located at $x = -0.8$. Due to the free surface boundary condition at $y = \pm 0.5$, surface waves develop

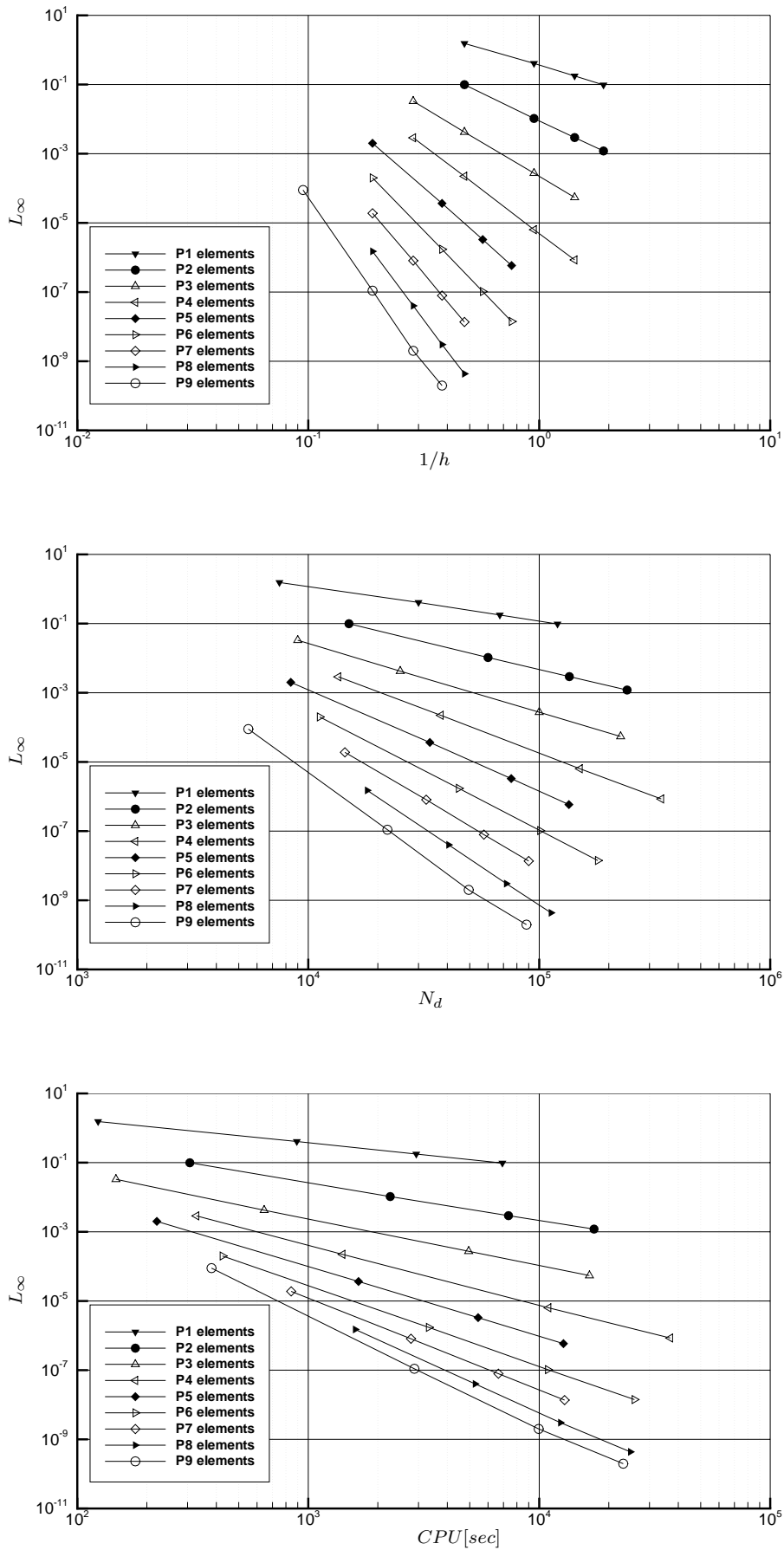


Figure 3. L_∞ error versus mesh width $1/h$, total number of degrees of freedom N_d and CPU time of ADER-DG schemes from $\mathcal{O}2 - \mathcal{O}10$ on the regular meshes.

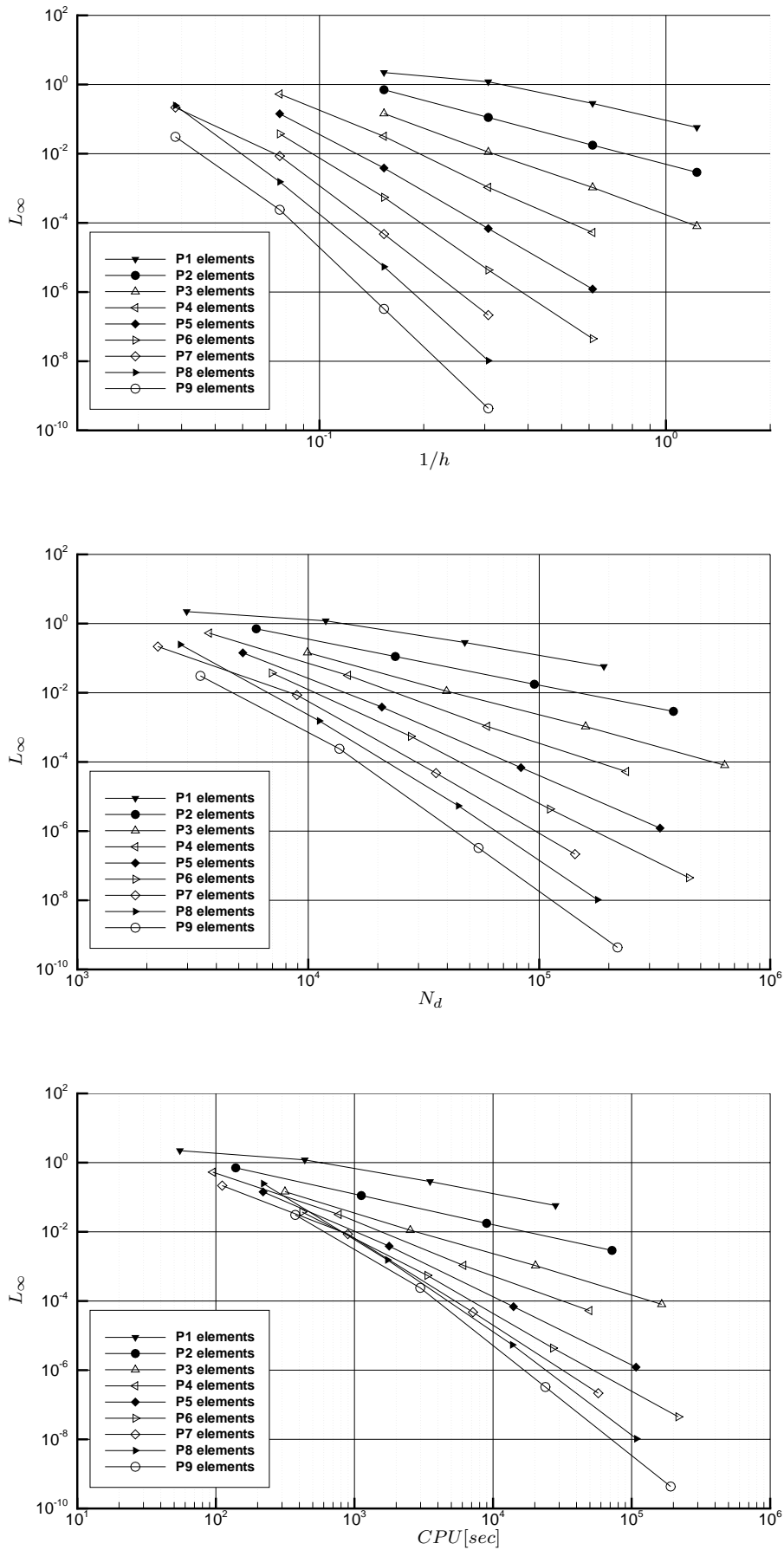


Figure 4. L_∞ error versus mesh width $1/h$, total number of degrees of freedom N_d and CPU time of ADER-DG schemes from $\mathcal{O}2 - \mathcal{O}10$ on the irregular meshes.

Table 1. Convergence rates from order 2 to 10 of ADER-DG on regular meshes.

h	L^∞	\mathcal{O}_{L^∞}	L^2	\mathcal{O}_{L^2}	N_d	CPU [s]
2.108	$1.542 \cdot 10^0$	—	$1.044 \cdot 10^2$	—	7500	123
1.054	$4.087 \cdot 10^{-1}$	1.916	$2.760 \cdot 10^1$	1.919	30000	892
0.703	$1.769 \cdot 10^{-1}$	2.065	$1.202 \cdot 10^1$	2.051	67500	2934
0.527	$9.733 \cdot 10^{-2}$	2.077	$6.657 \cdot 10^0$	2.053	120000	6925
2.108	$9.890 \cdot 10^{-2}$	—	$5.926 \cdot 10^0$	—	15000	307
1.054	$1.045 \cdot 10^{-2}$	3.242	$6.526 \cdot 10^{-1}$	3.183	60000	2263
0.703	$2.930 \cdot 10^{-3}$	3.137	$1.888 \cdot 10^{-1}$	3.059	135000	7358
0.527	$1.199 \cdot 10^{-3}$	3.105	$7.859 \cdot 10^{-2}$	3.046	240000	17269
3.514	$3.292 \cdot 10^{-2}$	—	$1.917 \cdot 10^0$	—	9000	147
2.108	$4.215 \cdot 10^{-3}$	4.024	$2.555 \cdot 10^{-1}$	3.945	25000	644
1.054	$2.734 \cdot 10^{-4}$	3.947	$1.633 \cdot 10^{-2}$	3.967	100000	4947
0.703	$5.444 \cdot 10^{-5}$	3.980	$3.243 \cdot 10^{-3}$	3.988	225000	16492
3.514	$2.887 \cdot 10^{-3}$	—	$1.254 \cdot 10^{-1}$	—	13500	328
2.108	$2.224 \cdot 10^{-4}$	5.018	$9.919 \cdot 10^{-3}$	4.967	37500	1408
1.054	$6.353 \cdot 10^{-6}$	5.129	$3.068 \cdot 10^{-4}$	5.015	150000	10971
0.703	$8.491 \cdot 10^{-7}$	4.964	$4.019 \cdot 10^{-5}$	5.013	337500	36923
5.270	$2.003 \cdot 10^{-3}$	—	$7.847 \cdot 10^{-2}$	—	8400	221
2.635	$3.665 \cdot 10^{-5}$	5.772	$1.411 \cdot 10^{-3}$	5.797	33600	1650
1.757	$3.299 \cdot 10^{-6}$	5.938	$1.285 \cdot 10^{-4}$	5.909	75600	5437
1.318	$5.851 \cdot 10^{-7}$	6.012	$2.315 \cdot 10^{-5}$	5.959	134400	12730
5.270	$2.004 \cdot 10^{-4}$	—	$7.096 \cdot 10^{-3}$	—	11200	425
2.635	$1.726 \cdot 10^{-6}$	6.859	$5.449 \cdot 10^{-5}$	7.025	44800	3323
1.757	$1.038 \cdot 10^{-7}$	6.934	$3.173 \cdot 10^{-6}$	7.013	100800	10886
1.318	$1.412 \cdot 10^{-8}$	6.934	$4.216 \cdot 10^{-7}$	7.016	179200	25834
5.270	$1.896 \cdot 10^{-5}$	—	$4.665 \cdot 10^{-4}$	—	14400	843
3.514	$8.074 \cdot 10^{-7}$	7.784	$1.955 \cdot 10^{-5}$	7.824	32400	2784
2.635	$7.903 \cdot 10^{-8}$	8.078	$2.010 \cdot 10^{-6}$	7.908	57600	6653
2.108	$1.365 \cdot 10^{-8}$	7.870	$3.449 \cdot 10^{-7}$	7.899	90000	12874
5.270	$1.505 \cdot 10^{-6}$	—	$3.256 \cdot 10^{-5}$	—	18000	1597
3.514	$4.003 \cdot 10^{-8}$	8.945	$8.438 \cdot 10^{-7}$	9.009	40500	5278
2.635	$3.036 \cdot 10^{-9}$	8.965	$6.434 \cdot 10^{-8}$	8.946	72000	12353
2.108	$4.342 \cdot 10^{-10}$	8.716	$7.396 \cdot 10^{-9}$	9.694	112500	24814
10.541	$8.902 \cdot 10^{-5}$	—	$1.660 \cdot 10^{-3}$	—	5500	381
5.270	$1.099 \cdot 10^{-7}$	9.662	$1.764 \cdot 10^{-6}$	9.879	22000	2878
3.514	$2.000 \cdot 10^{-9}$	9.882	$3.188 \cdot 10^{-8}$	9.898	49500	9946
2.635	$1.980 \cdot 10^{-10}$	8.038	$5.285 \cdot 10^{-9}$	6.246	88000	23100

right from the beginning of the simulation. When the planar wave hits the stiffer material of the inclusion at $x = -0.5$ at time $t = 0.15$, the elastic waves travel with 10 times higher velocities through the inclusion where they are reflected each time they hit either of the boundaries at $x = \pm 0.5$. Therefore the inclusion starts to vibrate, radiating waves of small amplitude into the outer material. Similar to LeVeque (2002) we use a nonlinear color scale in order to visualize also these waves with small amplitude.

In Fig. 5 we show two snapshots of the component σ_{xx} of the resulting wave field at simulation time $t = 0.3$. In the top figure, we used an ADER-DG $\mathcal{O}4$ scheme that uses 10 degrees of freedom per element. The corresponding mesh is constructed by using 200×100 squares in x - and y -direction, respectively, where each square is split into 4 similar triangles as shown in Fig. 2 a). Therefore the total number of triangles in the mesh is 80000.

In the bottom snapshot of Fig. 5, we used an ADER-DG $\mathcal{O}6$ scheme. The mesh spacing is now increased such that we only use 100×50 squares in x - and y -direction, respectively. Therefore the total number of triangles is only 20000 but due to the higher order of the scheme we now have 21 degrees of freedom per triangle, which finally roughly leads to half of the total number of degrees of freedom for the sixth order scheme. Comparing the measured CPU times of the fourth and the sixth order method we indeed get a two times lower CPU time for the computation with the ADER-DG $\mathcal{O}6$ scheme compared to the ADER-DG $\mathcal{O}4$ method. Visually comparing the snapshots in Fig. 5, one can hardly see any difference between the two results. In both cases all features of the solution are resolved equally well. Comparing our results qualitatively we get an excellent agreement with the solution of LeVeque (2002), who used a slightly different initial condition and a second order FV scheme on a 600×300 Cartesian grid. We note that for visualization of the results, the numerical solution is shown on a much finer grid than the one used for the computations. The visualization grid consists of about two million triangles at whose vertices the numerical solution of the ADER-DG schemes is evaluated according to (9).

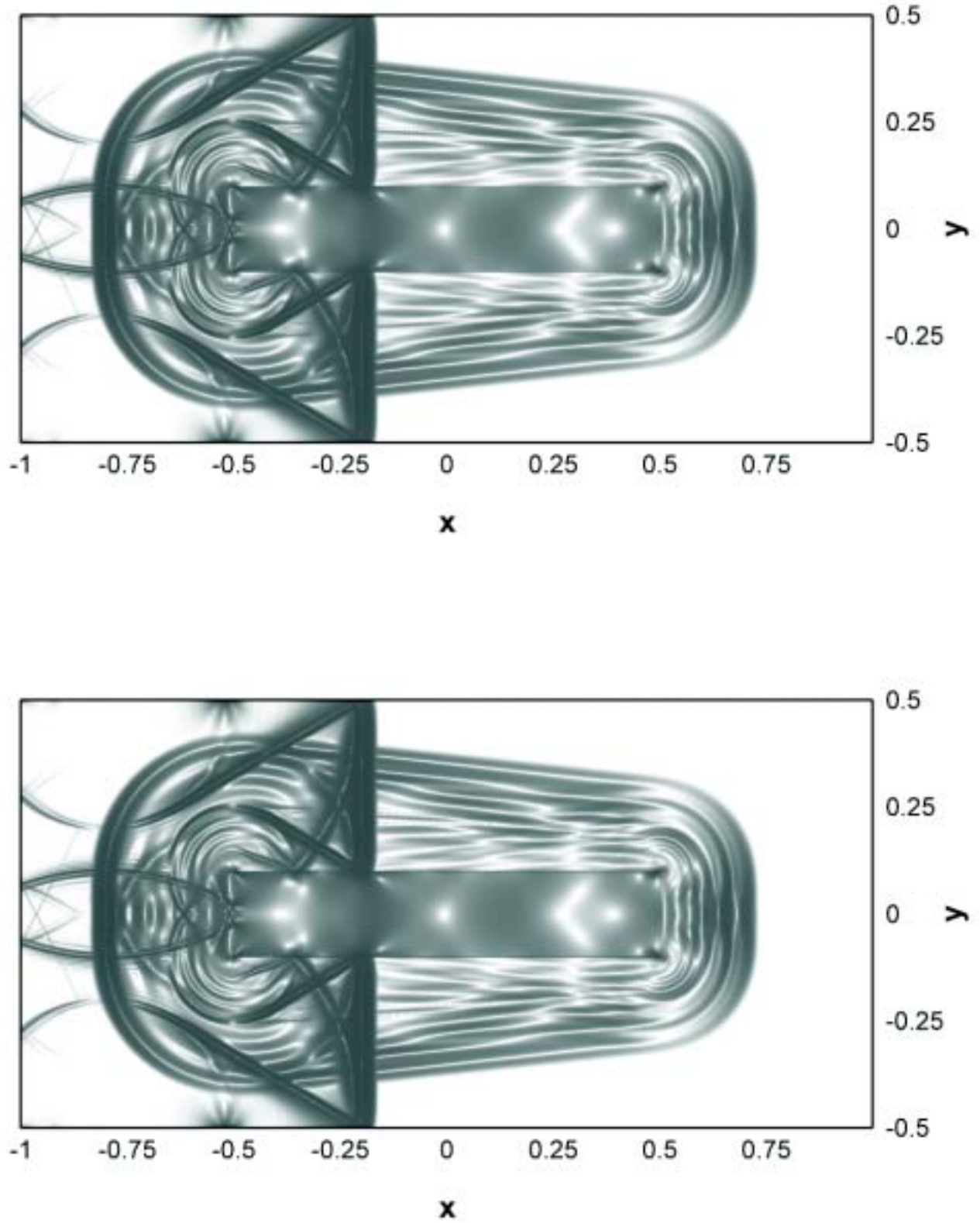


Figure 5. Stress component σ_{xx} at $t = 0.3$ for the inclusion test case. ADER-DG $\mathcal{O}4$ scheme with $4 \cdot 200 \times 100$ triangles (top), ADER-DG $\mathcal{O}6$ scheme with $4 \cdot 100 \times 50$ triangles (bottom).

Table 2. Convergence rates from order 2 to 10 of ADER-DG on the irregular meshes.

h	L^∞	\mathcal{O}_{L^∞}	L^2	\mathcal{O}_{L^2}	N_d	CPU [s]
6.513	$2.224 \cdot 10^0$	—	$1.459 \cdot 10^2$	—	2976	55
3.257	$1.201 \cdot 10^0$	0.889	$6.952 \cdot 10^1$	1.070	11904	438
1.628	$2.844 \cdot 10^{-1}$	2.078	$1.371 \cdot 10^1$	2.342	47616	3509
0.814	$5.748 \cdot 10^{-2}$	2.307	$2.704 \cdot 10^0$	2.342	190464	28232
6.513	$7.072 \cdot 10^{-1}$	—	$3.423 \cdot 10^1$	—	5952	139
3.257	$1.119 \cdot 10^{-1}$	2.660	$2.517 \cdot 10^0$	3.765	23808	1120
1.628	$1.758 \cdot 10^{-2}$	2.670	$2.373 \cdot 10^{-1}$	3.407	95232	8987
0.814	$2.894 \cdot 10^{-3}$	2.603	$2.814 \cdot 10^{-2}$	3.076	380928	72140
6.513	$1.447 \cdot 10^{-1}$	—	$1.768 \cdot 10^0$	—	9920	315
3.257	$1.111 \cdot 10^{-2}$	3.703	$9.910 \cdot 10^{-2}$	4.157	39680	2526
1.628	$1.054 \cdot 10^{-3}$	3.397	$6.604 \cdot 10^{-3}$	3.907	158720	20246
0.814	$8.002 \cdot 10^{-5}$	3.720	$4.266 \cdot 10^{-4}$	3.952	634880	164634
13.026	$5.288 \cdot 10^{-1}$	—	$5.660 \cdot 10^0$	—	3720	95
6.513	$3.166 \cdot 10^{-2}$	4.062	$1.384 \cdot 10^{-1}$	5.353	14880	771
3.257	$1.066 \cdot 10^{-3}$	4.893	$4.639 \cdot 10^{-3}$	4.899	59520	6123
1.628	$5.261 \cdot 10^{-5}$	4.340	$1.677 \cdot 10^{-4}$	4.789	238080	49648
13.026	$1.421 \cdot 10^{-1}$	—	$7.123 \cdot 10^{-1}$	—	5208	219
6.513	$3.845 \cdot 10^{-3}$	5.208	$1.279 \cdot 10^{-2}$	5.800	20832	1780
3.257	$6.839 \cdot 10^{-5}$	5.813	$2.255 \cdot 10^{-4}$	5.825	83328	14044
1.628	$1.220 \cdot 10^{-6}$	5.809	$3.892 \cdot 10^{-6}$	5.857	333312	107658
13.026	$3.750 \cdot 10^{-2}$	—	$1.569 \cdot 10^{-1}$	—	6944	419
6.513	$5.503 \cdot 10^{-4}$	6.091	$1.197 \cdot 10^{-3}$	7.034	27776	3352
3.257	$4.352 \cdot 10^{-6}$	6.982	$1.009 \cdot 10^{-5}$	6.891	111104	27034
1.628	$4.496 \cdot 10^{-8}$	6.597	$9.137 \cdot 10^{-8}$	6.787	444416	216821
26.052	$2.168 \cdot 10^{-1}$	—	$4.104 \cdot 10^0$	—	2232	111
13.026	$8.565 \cdot 10^{-3}$	4.662	$1.867 \cdot 10^{-2}$	7.780	8928	895
6.513	$4.746 \cdot 10^{-5}$	7.496	$9.682 \cdot 10^{-5}$	7.591	35712	7157
3.257	$2.154 \cdot 10^{-7}$	7.783	$4.058 \cdot 10^{-7}$	7.898	142848	57415
26.052	$2.481 \cdot 10^{-1}$	—	$1.509 \cdot 10^0$	—	2790	220
13.026	$1.540 \cdot 10^{-3}$	7.332	$3.697 \cdot 10^{-3}$	8.673	11160	1731
6.513	$5.397 \cdot 10^{-6}$	8.156	$7.347 \cdot 10^{-6}$	8.975	44640	13779
3.257	$1.040 \cdot 10^{-8}$	9.019	$1.981 \cdot 10^{-8}$	8.535	178560	108380
26.052	$3.077 \cdot 10^{-2}$	—	$3.504 \cdot 10^{-1}$	—	3410	374
13.026	$2.393 \cdot 10^{-4}$	7.006	$3.241 \cdot 10^{-4}$	10.078	13640	2981
6.513	$3.265 \cdot 10^{-7}$	9.518	$5.065 \cdot 10^{-7}$	9.322	54560	23859
3.257	$4.330 \cdot 10^{-10}$	9.559	$6.134 \cdot 10^{-9}$	6.368	218240	191180

From these results we conclude that for this example with strong jumps in the material properties the ADER-DG method behaves very robustly. Furthermore, confirming the results already obtained in the numerical convergence analysis in Section 5, we can see that in order to reach a certain resolution, less CPU time and also less memory is needed for higher order methods.

6.2 Example 2

In the second example we present the results of a global simulation of seismic waves, which is often problematic for many numerical methods due to the generation of an appropriate mesh. As FD schemes rely on a certain regularity of the mesh, spherical coordinates are often used. However, towards the center of the model, the mesh spacing decreases with depth such that the allowed time step decreases drastically and thus practical computations become difficult. Hence, regular meshes have to be recoarsened successively with depth and interpolation procedures are required to handle hanging nodes. Therefore, FD methods often are restricted to spherical sections, see e.g. (Igel 1999). Also the popular SEM relies on rather artificial mesh coarsening towards the center as shown in (Komatitsch & Tromp 2002).

In contrast, the proposed ADER-DG scheme on triangular meshes demonstrates a much higher flexibility concerning difficult geometries. Therefore, a circular geometry as needed for the discretization of the radially symmetric PREM of Dziewonski & Anderson (1981) does not impose any problems. As shown in Fig. 6 a triangular mesh can be built that respects the radial symmetry of the different layers of the PREM. Furthermore, the local mesh width can be adapted proportional to the local propagation speeds of the seismic waves. Hence, we chose larger triangular cell in areas with high wave speeds, e.g. in the lower mantle and small cells in low velocity zones, such as close to the surface or below the core-mantle boundary, where seismic wave speeds decrease dramatically. This way, the time step according to the local CFL

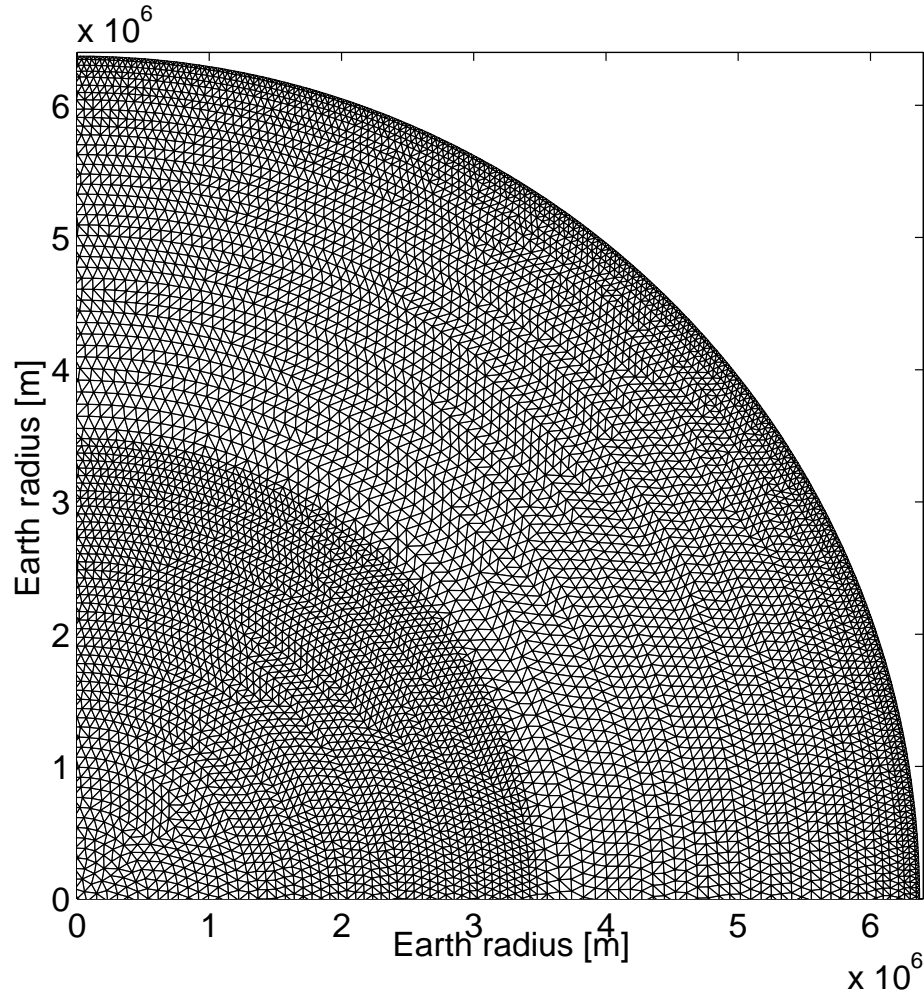


Figure 6. A quarter of the well adapted, velocity-dependent triangular mesh constructed for the simulation of global elastic wave propagation using PREM.

condition is used in an optimal sense.

As initial condition we use a Gaussian pulse in the two velocity components $Q_4 = u$ and $Q_5 = v$ given by

$$Q_{4,5}^0 = Q_{4,5}(\vec{x}, 0) = \vec{r}_{1,2} \exp\left(-\frac{1}{2} \frac{((x - x_G)^2 + (y - y_G)^2)}{\sigma^2}\right), \quad (50)$$

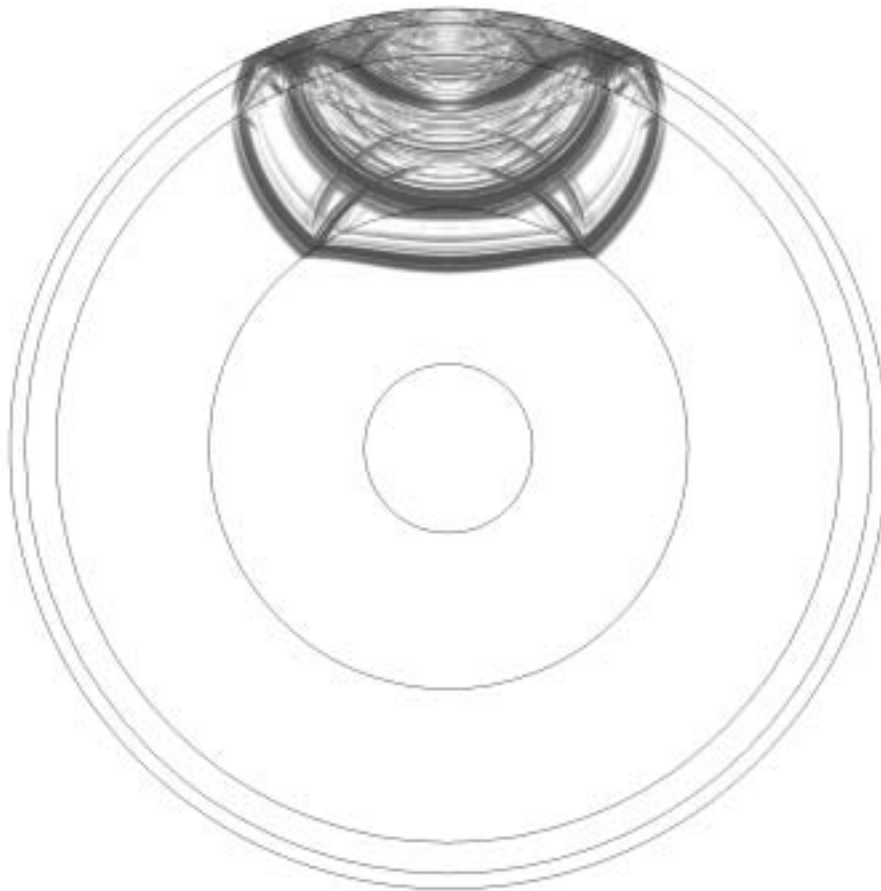
where the location $(x_G, y_G) = (0, 6 \cdot 10^6)$ is the center of the Gaussian pulse with a standard deviation of $\sigma = 5 \cdot 10^4$. The normalized vector

$$\vec{r}_{1,2} = ((x - x_G)^2 + (y - y_G)^2)^{-\frac{1}{2}} \cdot (x - x_G, y - y_G)^T \quad (51)$$

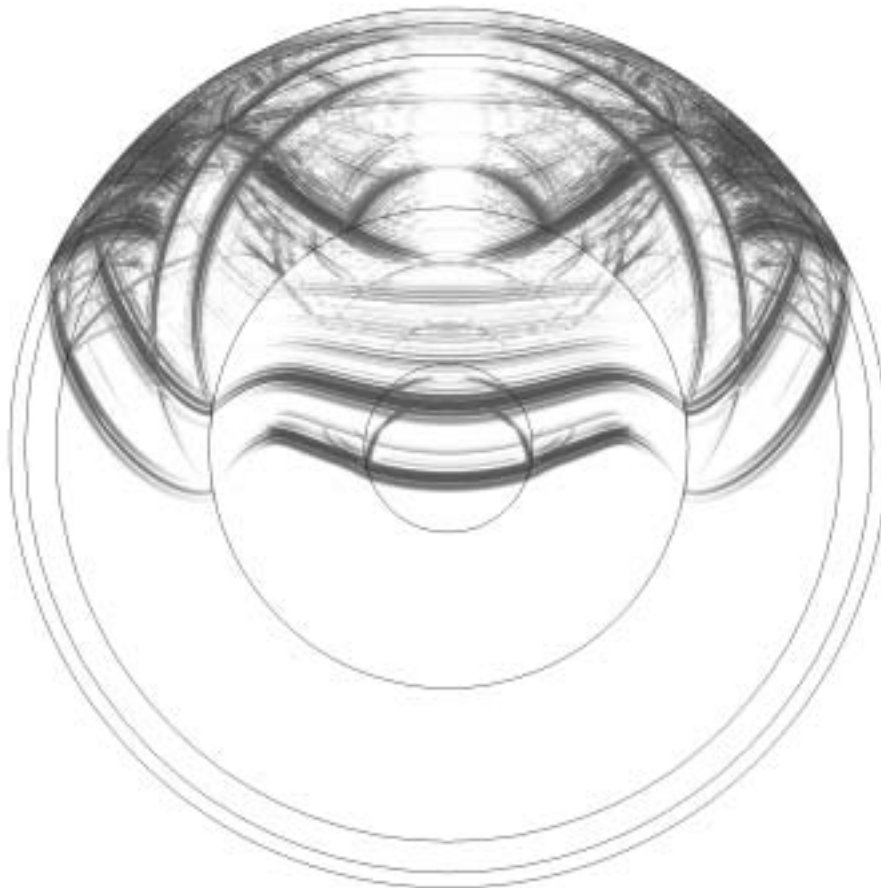
accounts for the dependency of the different velocity components on direction. This initial condition acts as an explosive seismic source at time $t = 0$, where a velocity perturbation is excited in radial direction.

In Figures 7 and 8 we show the wave field of the vertical velocity component w at four different times, after 300, 600, 900, and 1200 seconds. Again we use a non-linear color scale to visualize small amplitudes. At $t = 300$ s a strong reflection of P- and S-waves at the core-mantle boundary can be observed. At time $t = 600$ s the direct P-wave passes in inner core creating S-waves at the interface between outer and inner core. When the direct P-wave has passed the earth's inner and outer core at $t = 900$ s it leaves the inner, stiffer core vibrating. This result is similar to the observations of example 1 in Section 6.1. Furthermore, the shadowing effect of the core with respect to the direct wave can be seen clearly. At time $t = 1200$ s a complex wave pattern of reflected, transmitted and converted P- and S- waves has formed that interfere with each other and produce oscillations basically inside the whole earth.

We note that we do not compare the obtained results with reference solutions, as we only want to demonstrate the performance of the applied ADER-DG $\mathcal{O}6$ scheme on this problem. A comparison to reference solutions and measured data of real earthquake scenarios will follow in a subsequent publication where a fully three-dimensional model is used. However, we state that with the proposed ADER-DG scheme of high

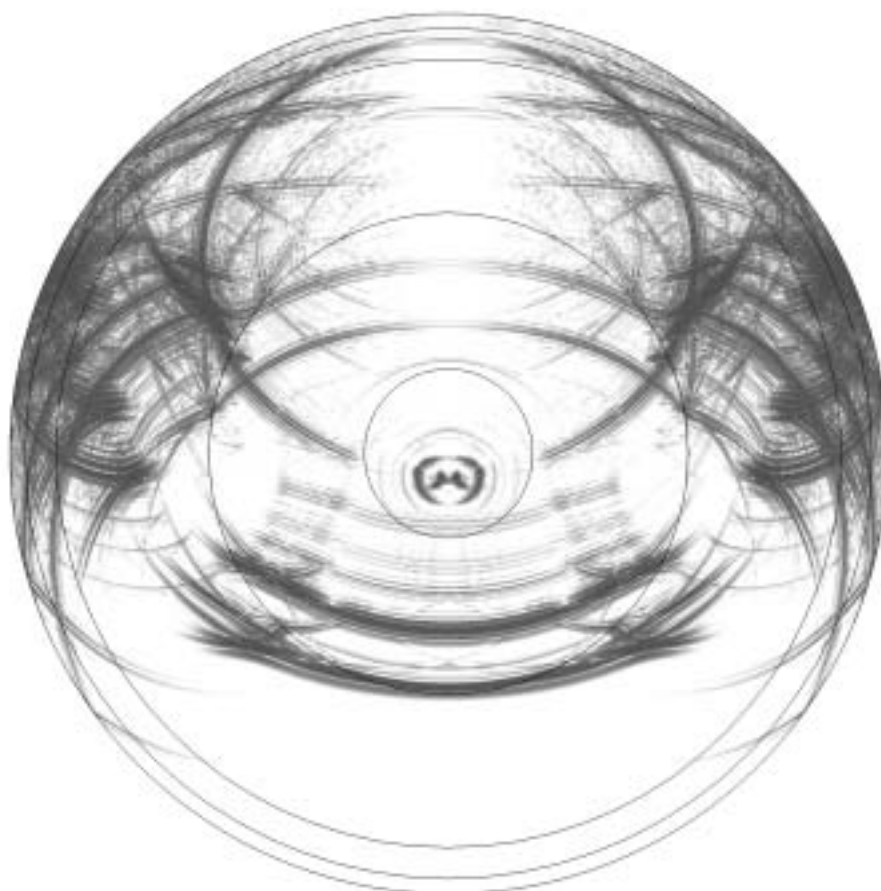


$t = 300$ s

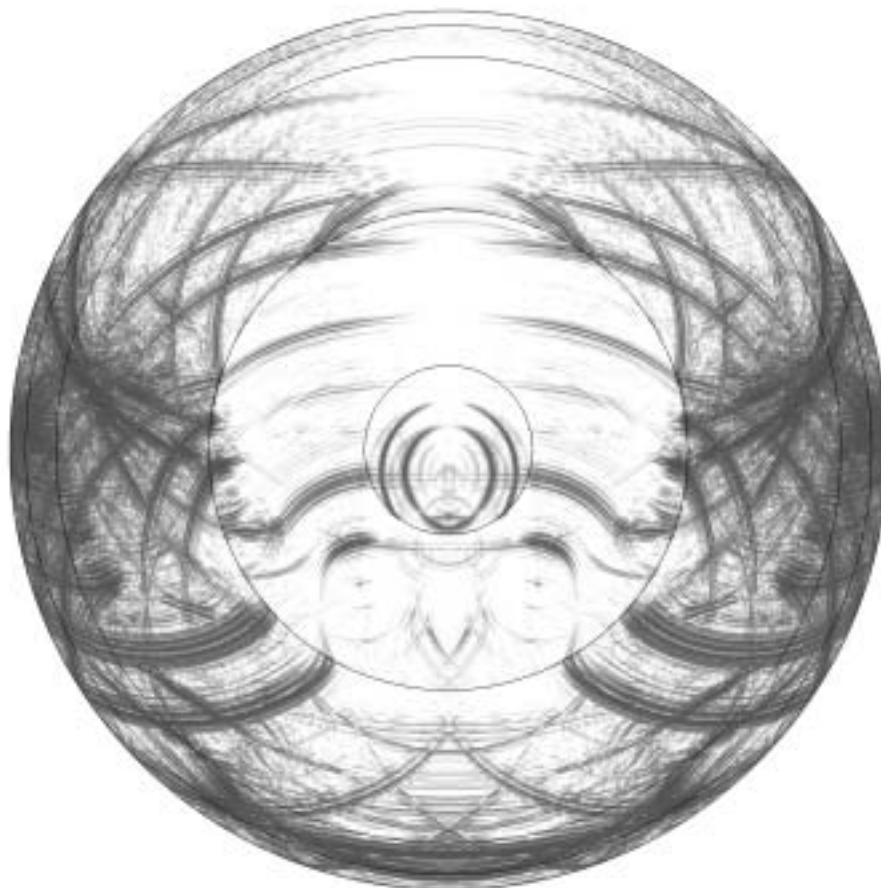


$t = 600$ s

Figure 7. Vertical velocity component w of the seismic wave field for the two-dimensional PREM after $t = 300$ s and $t = 600$ s.



$t = 900$ s



$t = 1200$ s

Figure 8. Vertical velocity component w of the seismic wave field for the two-dimensional PREM after $t = 900$ s and $t = 1200$ s.

order in space and time we still can resolve very fine features of the global wave field even after long simulation times when waves have propagated many wavelengths.

7 DISCUSSION AND CONCLUSIONS

We presented the mathematical details, convergence properties and applications of a new numerical approach, termed ADER-DG method, for the solution of the elastic wave equations on unstructured triangular meshes. The scope of this work has been to introduce and extend this arbitrarily high order accurate numerical method, originally developed in the field of computational fluid dynamics, to the community of numerical seismology in order to demonstrate its advantages to commonly used methods. As the amount and quality of information of the earth interior or of structures and properties of hydrocarbon reservoirs are growing rapidly and are becoming more detailed, it is of uttermost importance to develop computational tools that can use such models to compute highly accurate synthetic seismograms. In this work we described a numerical method that helps to reduce the numerical approximation error as much as possible, such that deviations from measured data have to originate basically from incorrect model parametrization. Therefore, in our opinion the new ADER-DG method can play a significant role for understanding the processes of wave propagation in complex, heterogeneous media as well as for model validation. In contrast to existing methods, the proposed ADER-DG scheme retains its high order accuracy and space and time even on unstructured meshes, which makes it particularly suited for problems of complicated geometry. We clearly could show that due to its sub cell resolution very coarse meshes can be used, which reduce the amount of required computer storage and allow for large time steps. Therefore, in contrast to the popular spectral element method, the computational efficiency of ADER-DG schemes increases with the order of accuracy. With the ongoing, rapidly growing computer power, the arbitrary high order of ADER-DG schemes provide a method, that will automatically follow these developments, such that we will always be able to reach machine precision just by increasing the desired order of accuracy. In addition, we demonstrated, that strong material heterogeneities, which often lead to problems in staggered finite difference schemes, can easily be handled, if element interfaces are aligned with the material boundary, as discontinuities of the numerical approximation are allowed between two adjacent elements.

We also claim that the proposed scheme is advantageous when considering anisotropic material. In fact, in this case only the entries of the Jacobian matrices have to be changed. Furthermore, an extension to unstructured tetrahedral meshes for full three-dimensional simulations has already been achieved. However, result on these topics will be presented in a further publication as this work was intended to give an introduction of the mathematical formulation of the ADER-DG approach and its applicability to problems of practical interest. The outlined principles in this paper can then be extended more easily to the three-dimensional and anisotropic case.

ACKNOWLEDGMENTS

The authors thank the DFG (Deutsche Forschungsgemeinschaft), as the work was supported through the *Emmy Noether-Programm* (KA 2281/1-1) and the DFG-CNRS research group FOR 508, *Noise Generation in Turbulent Flows*.

REFERENCES

- Aki, K. & Richards, P.G., 2002. *Quantitative Seismology*, University Science Books.
- Atkins, H. & Shu, C.W., 1998. Quadrature-free implementation of the Discontinuous Galerkin method for hyperbolic equations, *AIAA Journal*, **36**, 775-782.
- Bedford, A. & Drumheller, D.S., 1994. *Elastic Wave Propagation*, Wiley.
- Butcher, J.C., 1987. *The Numerical Analysis of Ordinary Differential Equations: Runge-Kutta and General Linear Methods*, Wiley.
- Carcione, J.M., 1994. The wave equation in generalised coordinates, *Geophysics*, **59**, 1911-1919.
- Cockburn, B., Karniadakis, G.E. & Shu, C.W., 2000. *Discontinuous Galerkin Methods, Theory, Computation and Applications*, LNCSE, **11**, Springer.
- Cockburn, B., Hou, S. & Shu, C.W., 1990. The Runge-Kutta local projection discontinuous Galerkin finite element method for conservation laws IV: the multidimensional case, *Math. Comp.*, **54**, 545-581.
- Cockburn, B., Lin, S.Y. & Shu, C.W., 1989. TVB Runge-Kutta local projection discontinuous Galerkin finite element method for conservation laws III: one dimensional systems, *J. Comput. Phys.*, **84**, 90-113.
- Cockburn, B. & Shu, C.W., 1989. TVB Runge-Kutta local projection discontinuous Galerkin finite element method for conservation laws II: general framework, *Math. Comp.*, **52**, 411-435.
- Cockburn, B. & Shu, C.W., 1991. The Runge-Kutta local projection P1-Discontinuous Galerkin finite element method for scalar conservation laws, *Mathematical Modelling and Numerical Analysis*, **25**, 337-361.
- Cockburn, B. & Shu, C.W., 1998. The Runge-Kutta discontinuous Galerkin method for conservation laws V: multidimensional systems, *J. Comput. Phys.*, **141**, 199-224.
- Dubiner, M., 1991. Spectral methods on triangles and other domains, *Journal of Scientific Computing*, **6**, 345-390.
- Dumbser, M., 2003. On the Improvement of Efficiency and Storage Requirements of the Discontinuous Galerkin Method for Aeroacoustics, *PAMM*, **3**, 426-427.
- Dumbser, M., 2005. Arbitrary High Order Schemes for the Solution of Hyperbolic Conservation Laws in Complex Domains, *PhD Thesis*, Universität Stuttgart, Institut für Aerodynamik und Gasdynamik.

- Dumbser, M. & Munz, C.D., 2005. Arbitrary High Order Discontinuous Galerkin Schemes, in *Numerical Methods for Hyperbolic and Kinetic Problems*, eds. Cordier, S., Goudon, T., Gutnic, M. & Sonnendruker, E., IRMA series in mathematics and theoretical physics, EMS Publishing House, 295–333.
- Dumbser, M., Schwartzkopff, T. & Munz, C.D. Arbitrary High Order Finite Volume Schemes for Linear Wave Propagation, to appear in *Notes on Numerical Fluid Mechanics and Multidisciplinary Design (NNFM)*, Springer.
- Dziewonski, A.M. & Anderson, D.L., 1981. Preliminary reference Earth model, *Physics of Earth and Planetary Interior*, **25**, 297-356.
- Fornberg, B., 1996. *A Practical Guide to Pseudospectral Methods*, Cambridge University Press, Cambridge.
- Hempel, D., 1995. Isotropic refinement and recoarsening in 2 dimensions, Technical Report, IB 223-95 A 35, DLR.
- Hughes, T.J.R., 1987. *The Finite Element Method - Linear Static and Dynamic Finite Element Analysis*, Prentice Hall.
- Igel, H., 1999. Wave propagation in three-dimensional spherical sections by the Chebyshev spectral method, *Geophys. J. Int.*, **136**, 559-566.
- Igel, H., Mora, P. & Riollot, B., 1995. Anisotropic wave propagation through finite-difference grids, *Geophysics*, **60**, 1203-1216.
- Käser, M. & Igel, H., 2001. Numerical simulation of 2D wave propagation on unstructured grids using explicit differential operators, *Geophys. Prosp.*, **49**, 607-619.
- Käser, M. & Igel, H., 2001. A comparative study of explicit differential operators on arbitrary grids, *J. Comput. Acoustics*, **9**, 1111-1125.
- Komatitsch, D. & Tromp, J., 1999. Introduction to the spectral-element method for 3-D seismic wave propagation, *Geophys. J. Int.*, **139**, 806-822.
- Komatitsch, D. & Tromp, J., 2002. Spectral-element simulations of global seismic wave propagation - I. Validation, *Geophys. J. Int.*, **149**, 390-412.
- Komatitsch, D. & Vilotte, J.P., 1998. The spectral-element method: an efficient tool to simulate the seismic response of 2D and 3D geological structures, *Bull. Seism. Soc. Am.*, **88**, 368-392.
- Levander, A.R., 1988. Fourth-order finite difference P-SV seismograms, *Geophysics*, **53**, 1425-1436.
- LeVeque, R.L., 2002. *Finite Volume Methods for Hyperbolic Problems*, Cambridge University Press, Cambridge.
- Meister, A. & Struckmeier, J., 2002. *Hyperbolic Partial Differential Equations: Theory, Numerics and Applications*, Vieweg, Braunschweig.
- Moczo, P., Kristek, J., Vavrycuk, V., Archuleta, R.J. & Halada, L., 2002. 3D heterogeneous staggered-grid finite-difference modeling of seismic motion with volume harmonic and arithmetic averaging of elastic moduli and densities, *Bull. Seism. Soc. Am.*, **92**, 3042-3066.
- Mora, P., 1989. Modeling anisotropic seismic waves in 3-D, *59th Ann. Int. Mtg Exploration Geophysicists, expanded abstracts*, 1039-1043.
- Patera, A.T., 1984. A spectral-element method for fluid dynamics: laminar flow in a channel expansion, *J. Comput. Phys.*, **144**, 45-58.
- Priolo, E., Carcione, J.M. & Seriani, G., 1994. Numerical simulation of interface waves by high-order spectral modeling techniques, *J. acoust. Soc. Am.*, **95**, 681-693.
- Reed, W.H. & Hill, T.R., 1973. Triangular mesh methods for the neutron transport equation, Technical Report, LA-UR-73-479, Los Alamos Scientific Laboratory.
- Schwartzkopff, T., Munz, C.D. & Toro, E.F., 2002. ADER: A High-Order Approach for Linear Hyperbolic Systems in 2D, *J. Sci. Comput.*, **17**, 231-240.
- Schwartzkopff, T., Dumbser, M. & Munz, C.D., 2004. Fast high order ADER schemes for linear hyperbolic equations, *J. Comput. Phys.*, **197**, 532-539.
- Schwarz, H.R., 1988. *Finite Element Methods*, Academic Press, London.
- Seriani, G., 1998. 3-D large-scale wave propagation modeling by a spectral-element method on a Cray T3E multiprocessor, *Comput. Methods Appl. Mech. Eng.*, **164**, 235-247.
- Tessmer, E., 1995. 3-D Seismic modelling of general material anisotropy in the presence of the free surface by a Chebyshev spectral method, *Geophys. J. Int.*, **121**, 557-575.
- Tessmer, E., 1995. 3-D elastic modelling with surface topography by a Chebyshev spectral method, *Geophysics*, **59**, 464-473.
- Titarev, V.A. & Toro, E.F., 2002. ADER: Arbitrary high order Godunov approach, *J. Sci. Comput.*, **17**, 609-618.
- Toro, E.F., Millington, A.C. & Nejad, L.A., 2001. Towards very high order Godunov schemes, in *Godunov methods; Theory and applications*, Kluwer Academic Plenum Publishers, Oxford, 907-940.
- Toro, E.F. & Titarev, V.A. 2002. Solution of the generalized Riemann problem for advection-reaction equations, *Proc. Roy. Soc. London*, 271-281.
- Virieux, J., 1984. SH-wave propagation in heterogeneous media: Velocity-stress finite-difference method, *Geophysics*, **49**, 1933-1942.
- Virieux, J., 1986. P-SV wave propagation in heterogeneous media: Velocity-stress finite-difference method, *Geophysics*, **51**, 889-901.

LIST OF FIGURES

- 1 Transformation from the physical triangle $\mathcal{T}^{(m)}$ to the canonical reference triangle \mathcal{T}_E with nodes $(0, 0)$, $(1, 0)$ and $(0, 1)$.
- 2 Meshes for the analysis of the numerical convergence orders: a) regular mesh, b) refined regular mesh c) irregular mesh, d) refined irregular mesh.
- 3 L^∞ error versus mesh width $1/h$, total number of degrees of freedom N_d and CPU time of ADER-DG schemes from $\mathcal{O}2 - \mathcal{O}10$ on the regular meshes.
- 4 L^∞ error versus mesh width $1/h$, total number of degrees of freedom N_d and CPU time of ADER-DG schemes from $\mathcal{O}2 - \mathcal{O}10$ on the irregular meshes.
- 5 Stress component σ_{xx} at $t = 0.3$ for the inclusion test case.
ADER-DG $\mathcal{O}4$ scheme with $4 \cdot 200 \times 100$ triangles (top),
ADER-DG $\mathcal{O}6$ scheme with $4 \cdot 100 \times 50$ triangles (bottom).
- 6 A quarter of the well adapted, velocity-dependent triangular mesh constructed for the simulation of global elastic wave propagation using PREM.
- 7 Vertical velocity component w of the seismic wave field for the two-dimensional PREM after $t = 300s$ and $t = 600s$.
- 8 Vertical velocity component w of the seismic wave field for the two-dimensional PREM after $t = 900s$ and $t = 1200s$.